

# **Electronic Structure, mass fluctuation, and Localized Bond Properties of two-dimensional double-layer transition metal chalcogenide $\text{MX}_2$ (M = Mo, W; X = S, Se, Te) Calculated Based on Density Functional Theory and BBC model**

Yaorui Tan and Maolin Bo\*

Key Laboratory of Extraordinary Bond Engineering and Advanced Materials  
Technology (EBEAM) of Chongqing, Yangtze Normal University, Chongqing 408100,  
China

\*Author to whom any correspondence should be addressed.  
(E-mail addresses: bmlwd@yznu.edu.cn)

## **Abstract**

This study systematically investigates the electronic structure and bonding properties of two-dimensional bilayer transition metal chalcogenides  $\text{MX}_2$  (M = Mo, W; X = S, Se, Te) using density functional theory calculations. Through the analysis of band gaps, deformation bond energies, and non-Hermitian bonding characteristics of various  $\text{MX}_2$  compounds, the electronic properties and chemical bonding features are comprehensively examined. The findings demonstrate that charge transfer plays a critical role in electron mass fluctuation, with the incorporation of topological geometric analysis confirming the influence of mass changes on atomic bonding and electronic states. Furthermore, Heterojunctions between distinct atomic layers are shown to effectively modulate the band gap of two-dimensional bilayer transition metal chalcogenides. This work establishes a theoretical foundation for advancing the application of these materials.

**Keywords:** Transition metal chalcogenide, Non-Hermitian bonding, Fluctuation of electron mass

## 1. Introduction

With the widespread application of two-dimensional materials in electronics, optics, and catalysis, transition metal chalcogenides  $\text{MX}_2$  ( $\text{M} = \text{Mo}, \text{W}; \text{X} = \text{S}, \text{Se}, \text{Te}$ ) have emerged as a focal point of research due to their unique physical and chemical properties. For instance, transition metal chalcogenide heterojunctions, utilized as electrode materials in lithium-ion batteries[1, 2], effectively enhance the structural stability and conductivity of the materials, significantly enhancing the specific capacity and cycling performance of the batteries. Additionally, materials such as molybdenum disulfide ( $\text{MoS}_2$ ), with relatively large interlayer spacing, facilitate lithium-ion intercalation and deintercalation, demonstrating excellent performance in battery applications[3-5]. In addition, transition metal chalcogenide heterojunctions show great potential in photocatalysis[6-8], as they can promote water splitting to generate hydrogen and oxygen, achieving effective conversion of solar energy into chemical energy. Constructing heterojunctions enhances the separation efficiency of photogenerated charge carriers [9, 10], improving photocatalytic activity and offering innovative solutions for clean energy production. Furthermore, these materials are also used as light-absorbing layers in solar cells[11], where their tunable bandgap and excellent light absorption properties allow for the optimization of energy band structures, thereby improving the photovoltaic conversion efficiency. By varying the types of transition metals and chalcogen elements and adjusting the stacking of atomic layers, the bandgap of these materials can be precisely controlled, offering theoretical guidance for designing diverse optoelectronic devices[12-15]. Therefore, transition metal chalcogenide heterojunctions not only have significant applications in energy storage and optoelectronics but also offer vast prospects for the innovation and development of related technologies.

This study employs density functional theory (DFT) and the Binding Energy and Bond Charge (BBC) model[16] to analyze the band structure, density of states, and atomic bonding in two-dimensional bilayer  $\text{MX}_2$  compounds. The band gaps of the heterostructures  $\text{MoS}_2/\text{WSe}_2$ ,  $\text{MoS}_2/\text{MoTe}_2$ , and  $\text{WSe}_2/\text{MoTe}_2$  [17-20] were determined to be 0.934 eV, 0.100 eV and 0.334 eV, respectively, while the band gaps of the bilayer  $\text{WS}_2$ ,  $\text{WSe}_2$ , and  $\text{WTe}_2$  [21-23] were 1.838 eV, 1.496 eV, and 0.917 eV. These findings underscore the significant variability in band gaps, emphasizing the capacity of interlayer heterostructures to modulate the bandgap of two-dimensional transition metal dichalcogenides. Furthermore, calculations of electron transfer and atomic

bonding demonstrate that charge transfer is intricately linked to electronic mass fluctuations, indicating that such variations profoundly influence atomic bonding and the overall electronic structure.

## 2. Methods

### 2.1 DFT calculations

The electronic properties and structural relaxation of MoS<sub>2</sub>/WSe<sub>2</sub>, MoS<sub>2</sub>/MoTe<sub>2</sub>, WSe<sub>2</sub>/MoTe<sub>2</sub>, WS<sub>2</sub>, WSe<sub>2</sub>, and WTe<sub>2</sub> were simulated using the Cambridge Sequential Total Energy Package (CASTEP). This package employs DFT with a plane wave pseudopotential and HSE06 to describe electron exchange and related potentials[24]. The calculations examined the energy, structure, bonding, and electronic properties of the aforementioned compounds: MoS<sub>2</sub>/WSe<sub>2</sub>, MoS<sub>2</sub>/MoTe<sub>2</sub>, WSe<sub>2</sub>/MoTe<sub>2</sub>, WS<sub>2</sub>, WSe<sub>2</sub>, and WTe<sub>2</sub>. the TS scheme was applied for DFT-D dispersion correction to account for long-range vdW interactions. The cut-off energies, band gaps, and *k*-point grids utilized in this study are presented in **Table 1**. All structures were fully optimized without any symmetry constraints until the forces were reduced to less than 0.01 eV/Å, and the energy tolerance decreased below 5.0×10<sup>-6</sup> eV the specified threshold per atom. For self-consistent field calculations, A convergence threshold 1.0×10<sup>-6</sup> eV per atom was employed for MoS<sub>2</sub>/WSe<sub>2</sub>, MoS<sub>2</sub>/MoTe<sub>2</sub>, WSe<sub>2</sub>/MoTe<sub>2</sub>, WS<sub>2</sub>, WSe<sub>2</sub>, and WTe<sub>2</sub>.

**Table 1** Cut-off energies, bandgaps, and *k*-points of MoS<sub>2</sub>/WSe<sub>2</sub>, MoS<sub>2</sub>/MoTe<sub>2</sub>, WSe<sub>2</sub>/MoTe<sub>2</sub>, WS<sub>2</sub>, WSe<sub>2</sub> and WTe<sub>2</sub>

	Cut-off energy	<i>k</i> -point	Band gap (HSE06)
MoS <sub>2</sub> /WSe <sub>2</sub>	650.0 eV	15×15×2	0.934 eV
MoS <sub>2</sub> /MoTe <sub>2</sub>	650.0 eV	15×15×2	0.100 eV
WSe <sub>2</sub> /MoTe <sub>2</sub>	650.0 eV	15×15×2	0.334 eV
WS <sub>2</sub>	650.0 eV	15×15×2	1.838 eV
WSe <sub>2</sub>	650.0 eV	15×15×2	1.496 eV
WTe <sub>2</sub>	650.0 eV	15×15×2	0.917 eV

### 2.2. BBC model

The BBC model[16] consists of the binding energy model (BC), bond charge model (BC), and the Hamiltonian of the BB model.

$$H = \xi(0) \sum_I \hat{n}_I - t \sum_I \sum_{\rho} C_I^+ C_{I+\rho} = (E_n^a - \gamma^m A_n) \sum_I \hat{n}_I - t \sum_I \sum_{\rho} C_I^+ C_{I+\rho} \quad (1)$$

$\hat{n}_I$  represents the electron number operator in the wanier representation. So, it

$\sum_I \hat{n}_I = C_I^+ C_I$  can be obtained.  $A_n$  represents the energy shift,  $E_n^a$  is the atomic

energy level, and  $t$  is called the overlapping integral.

$$\begin{cases} A_n = -\int a_n^*(\vec{r}-\vec{l}) [V(\vec{r}) - v_a(\vec{r}-\vec{l})] a_n(\vec{r}-\vec{l}) d\vec{r} \\ E_n^a = \int a_n^*(\vec{r}-\vec{l}) \left[ -\frac{\hbar^2}{2m} \nabla^2 + v_a(\vec{r}-\vec{l}) \right] a_n(\vec{r}-\vec{l}) d\vec{r} \\ t = \sum_{l,l'} C_l^+ C_{l'} \int a^*(\vec{r}-\vec{l}) [V(\vec{r}) - v_a(\vec{r}-\vec{l})] a(\vec{r}-\vec{l}') d\vec{r} \end{cases} \quad (2)$$

$\xi(0)$  is the local orbital electron energy. Therefore, there exists

$\xi(0) = (E_n^a - A_n)$ .  $E_n^a$  caused by the potential of  $N-1$  atoms outside the lattice point  $l$  in the lattice  $V(r)$  is the potential and  $v_a(\vec{r}-\vec{l})$  is the atomic potential.

The binding energy (BE) shifts of the bulk and surface atoms can be expressed as:

$$\Delta E_v(B) = A_n \sum_l \hat{n}_l, \quad \Delta E_v(i) = \gamma^m A_n \sum_l \hat{n}_l, \quad (3)$$

For chemical bonding, **Eq. 2** can be written as:

$$\gamma^m = \frac{E_v(i) - E_v(0)}{E_v(B) - E_v(0)} = \left( \frac{E_v(x) - E_v(0)}{E_v(B) - E_v(0)} \right)^m \approx \left( \frac{Z_x d_b}{Z_b d_x} \right)^m = \left( \frac{Z_b - \sigma'_i}{Z_b} \right)^m \left( \frac{d_x}{d_b} \right)^{-m} \approx \left( \frac{d_x}{d_b} \right)^{-m} \quad (4)$$

$\sigma'$  is very small; therefore  $(Z_b - \sigma')/Z_b \approx 1$ , For metal  $m =$

$$1, \left( \frac{Z_b - \sigma'_i}{Z_b} \right)^m \left( \frac{d_x}{d_b} \right)^{-m} = \left( \frac{d_x}{d_b} \right)^{-m'} \quad \text{obtain } m' = m \left( 1 - \frac{\ln \frac{Z_b - \sigma'_i}{Z_b}}{\ln \left( \frac{d_x}{d_b} \right)} \right). \text{ For example, we}$$

calculate the energy level shift of Mo 3d,  $E_v(B) = 227.569$  eV,  $E_v(x) = 227.957$  eV,

$\frac{d_x}{d_b} = 0.875$ ; We use  $E_i = -13.6 \frac{(Z - \sigma_i)^2}{n^2}$ , considering the influence of angular

momentum  $E_i(x) = -13.6 \frac{(Z - \sigma_i)^2}{(n + 0.7 * l)^2}$ ,  $Z = 42$ ,  $n = 3$ ,  $l = 2$ . For the orbital energy of

Mo 3d:  $E_{3d}(x) = -13.6 \frac{(42 - \sigma_i)^2}{(3 + 0.7 * 2)^2}$ ,  $\sigma_B = 24.001$  eV,  $\sigma_x = 23.986$  eV,  $\sigma'_i = 0.015$ ,

$m' = 0.995 \approx 1$ . Therefore  $m \approx m'$ .

The Hamiltonian of a system in the BC model is expressed as:

$$H = \sum_{k\sigma} \frac{\hbar^2 k^2}{2m} a_{k\sigma}^\dagger a_{k\sigma} + \frac{e_1^2}{2V} \sum_q^* \sum_{\bar{k}\sigma} \sum_{\bar{k}'\lambda} \frac{4\pi}{q^2} a_{\bar{k}+\bar{q},\sigma}^\dagger a_{\bar{k}'-\bar{q},\lambda}^\dagger a_{\bar{k}'\lambda} a_{\bar{k}\sigma} \quad (5)$$

The electron-interaction terms for density fluctuations, which are primarily caused by electrostatic shielding through electron exchange, are given by:

$$\begin{aligned} \Delta V &= V_{ee} - V'_{ee} \\ &= \frac{e_1^2}{2V} \sum_q^* \sum_{\bar{k}\sigma} \sum_{\bar{k}'\lambda} \frac{4\pi}{q^2} a_{\bar{k}+\bar{q},\sigma}^\dagger a_{\bar{k}'-\bar{q},\lambda}^\dagger a_{\bar{k}'\lambda} a_{\bar{k}\sigma} - \frac{e_1^2}{2V} \sum_k \sum_{\bar{k}'} \sum_{\bar{q}} \sum_{\sigma\lambda} \frac{4\pi}{q^2 + \mu^2} a_{\bar{k}+\bar{q},\sigma}^\dagger a_{\bar{k}'-\bar{q},\lambda}^\dagger a_{\bar{k}'\lambda} a_{\bar{k}\sigma} \\ &= \frac{1}{4\pi\epsilon_0} \frac{e^2}{2|\bar{r}-\bar{r}'|} \int d^3r \int d^3r' \rho(\bar{r}) \rho(\bar{r}') e^{-\mu(\bar{r}-\bar{r}')} \end{aligned}$$

Then, we

have:

$$\begin{aligned} \delta V_{bc} &= V'_{ee1} - V'_{ee2} \\ &= \frac{e_1^2}{2V} \sum_k \sum_{\bar{k}'} \sum_{\bar{q}} \sum_{\sigma\lambda} \frac{4\pi}{q^2 + \mu_1^2} a_{\bar{k}+\bar{q},\sigma}^\dagger a_{\bar{k}'-\bar{q},\lambda}^\dagger a_{\bar{k}'\lambda} a_{\bar{k}\sigma} - \frac{e_1^2}{2V} \sum_k \sum_{\bar{k}'} \sum_{\bar{q}} \sum_{\sigma\lambda} \frac{4\pi}{q^2 + \mu_2^2} a_{\bar{k}+\bar{q},\sigma}^\dagger a_{\bar{k}'-\bar{q},\lambda}^\dagger a_{\bar{k}'\lambda} a_{\bar{k}\sigma} \\ &= \frac{e_1^2}{2V} \sum_q^* \sum_{\bar{k}\sigma} \sum_{\bar{k}'\lambda} \frac{4\pi}{q^2} a_{\bar{k}+\bar{q},\sigma}^\dagger a_{\bar{k}'-\bar{q},\lambda}^\dagger a_{\bar{k}'\lambda} a_{\bar{k}\sigma} - \frac{1}{4\pi\epsilon_0} \frac{e^2}{2|\bar{r}-\bar{r}'|} \int d^3r \int d^3r' \rho(\bar{r}) \rho(\bar{r}') e^{-\mu_1(\bar{r}-\bar{r}')} \\ &\quad - \frac{e_1^2}{2V} \sum_q^* \sum_{\bar{k}\sigma} \sum_{\bar{k}'\lambda} \frac{4\pi}{q^2} a_{\bar{k}+\bar{q},\sigma}^\dagger a_{\bar{k}'-\bar{q},\lambda}^\dagger a_{\bar{k}'\lambda} a_{\bar{k}\sigma} + \frac{1}{4\pi\epsilon_0} \frac{e^2}{2|\bar{r}-\bar{r}'|} \int d^3r \int d^3r' \rho(\bar{r}) \rho(\bar{r}') e^{-\mu_2(\bar{r}-\bar{r}')} \\ &= -\frac{1}{4\pi\epsilon_0} \frac{e^2}{2|\bar{r}-\bar{r}'|} \int d^3r \int d^3r' \rho(\bar{r}) \rho(\bar{r}') e^{-\mu_1(\bar{r}-\bar{r}')} + \frac{1}{4\pi\epsilon_0} \frac{e^2}{2|\bar{r}-\bar{r}'|} \int d^3r \int d^3r' \rho(\bar{r}) \rho(\bar{r}') e^{-\mu_2(\bar{r}-\bar{r}')} \end{aligned} \quad (6)$$

Regarding the charge density fluctuations, use the following formula:

$$\rho(\bar{r}) \rho(\bar{r}') (e^{-\mu_2(\bar{r}-\bar{r}')} - e^{-\mu_1(\bar{r}-\bar{r}')} ) = \delta\rho(\bar{r}) \delta\rho(\bar{r}') = (\rho(\bar{r}) - \sum_i \rho_i) (\rho(\bar{r}') - \sum_j \rho_j)$$

$$(e^{-\mu_2(\bar{r}-\bar{r}')} - e^{-\mu_1(\bar{r}-\bar{r}')} ) = (1 - \frac{\sum_i \rho_i}{\rho(\bar{r})}) (1 - \frac{\sum_j \rho_j}{\rho(\bar{r}')})$$

The deformation bond

Among them,

energy  $\delta V_{bc}$  is represented by Equation 7:

$$\delta V_{bc} = \frac{1}{4\pi\epsilon_0} \frac{e^2}{2|\bar{r}-\bar{r}'|} \int d^3r \int d^3r' \delta\rho(\bar{r}) \delta\rho(\bar{r}')$$

(7)

Also,  $\delta\rho$  satisfies the conditions outlined in Equation 8:

$$\left( \delta\rho_{\text{Hole-electron}} \leq \delta\rho_{\text{Antibonding-electron}} < \delta\rho_{\text{No charge transfer}} = 0 < \delta\rho_{\text{Nonbonding-electron}} \leq \delta\rho_{\text{Bonding-electron}} \right) \quad (8)$$

For atomic (strong) bonding states:

$$\delta\rho_{\text{Hole-electron}}(\vec{r}) \delta\rho_{\text{Bonding-electron}}(\vec{r}') < 0 (\text{Strong Bonding}) \quad (9)$$

For atomic nonbonding or weak-bonding states:

$$\left\{ \begin{array}{l} \delta\rho_{\text{Hole-electron}}(\vec{r}) \delta\rho_{\text{Nonbonding-electron}}(\vec{r}') < 0 (\text{Nonbonding or Weak Bonding}) \\ \delta\rho_{\text{Antibonding-electron}}(\vec{r}) \delta\rho_{\text{Bonding-electron}}(\vec{r}') < 0 (\text{Nonbonding or Weak Bonding}) \\ \delta\rho_{\text{Antibonding-electron}}(\vec{r}) \delta\rho_{\text{Nonbonding-electron}}(\vec{r}') < 0 (\text{Nonbonding}) \end{array} \right. \quad (10)$$

For atomic antibonding states:

$$\left\{ \begin{array}{l} \delta\rho_{\text{Nonbonding-electron}}(\vec{r}) \delta\rho_{\text{Bonding-electron}}(\vec{r}') > 0 (\text{Antibonding}) \\ \delta\rho_{\text{Hole-electron}}(\vec{r}) \delta\rho_{\text{Antibonding-electron}}(\vec{r}') > 0 (\text{Antibonding}) \\ \delta\rho_{\text{Hole-electron}}(\vec{r}) \delta\rho_{\text{Hole-electron}}(\vec{r}') > 0 (\text{Antibonding}) \\ \delta\rho_{\text{Antibonding-electron}}(\vec{r}) \delta\rho_{\text{Antibonding-electron}}(\vec{r}') > 0 (\text{Antibonding}) \\ \delta\rho_{\text{Nonbonding-electron}}(\vec{r}) \delta\rho_{\text{Nonbonding-electron}}(\vec{r}') > 0 (\text{Antibonding}) \\ \delta\rho_{\text{Bonding-electron}}(\vec{r}) \delta\rho_{\text{Bonding-electron}}(\vec{r}') > 0 (\text{Antibonding}) \end{array} \right. \quad (11)$$

The formation of chemical bonds is related to fluctuations in electron density  $\delta\rho$ .

### 2.3 Riemann sphere and Möbius transformation

In Euclidean space  $R^3$ , the complex number set  $C$  is represented as the  $XY$ -plane[25]. A sphere  $S$  is defined with center at  $(0,0,1/2)$  and radius  $1/2$ , with the north pole  $N = (0,0,1)$  as its vertex. The point  $W = (X, Y, Z)$  lies on the surface of sphere  $S$ , and the line connecting  $N$  and  $W$  intersects the  $XY$ -plane at the projection point  $w = x + iy$ . Conversely, a line from the point  $w = (x, y, 0)$  in the complex plane to  $N$  intersects the sphere at a unique point  $W$ . As shown in **Fig. 1**.

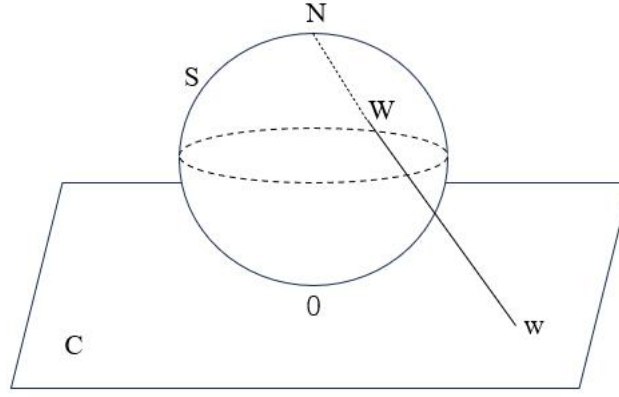


**Fig. 1** Riemann sphere  $S$  and projection

This geometric explanation provides an objective representation of a point on a perforated spherical surface  $S$  and a complex plane. The analytical description of this objective representation is as follows.

$$x = \frac{X}{1-Z}, \quad y = \frac{Y}{1-Z} \quad (12)$$

Substituting  $W$  with  $w$ :

$$Y = \frac{y}{x^2 + y^2 + 1}, \quad X = \frac{x}{x^2 + y^2 + 1}, \quad Z = \frac{x^2 + y^2}{x^2 + y^2 + 1} \quad (13)$$

The complex plane can cover the sphere, and a rational function defined on the extended complex plane can be viewed as a mapping of the sphere onto itself, transforming the pole into the north pole  $N$ . The Riemann sphere provides a powerful geometric framework for the relationship between the complex set and rational functions.

The Möbius transformation[26] maps a point  $z$  on the complex plane, expressed as  $M(z) = \frac{az+b}{cz+d}$  with complex numbers  $a$ ,  $b$ ,  $c$ , and  $d$  (where  $ad - bc \neq 0$ ). It is regarded as a fractional linear function that uniquely maps each point on the complex plane. Each Möbius transformation  $M(z)$  corresponds to a  $(2 \times 2)$  matrix,  $[M]$ , with complex elements:

$$M(z) = \frac{az+b}{cz+d} \rightarrow [M] = \begin{bmatrix} a & b \\ c & d \end{bmatrix} \quad (14)$$

To visualize the Möbius transformation  $M(z) = \frac{az+b}{cz+d}$ , we assume it has two fixed points  $\xi_{\pm}$  and consider it a mapping of itself  $z \mapsto \omega = M(z)$ , as shown in **Fig. 2a**.

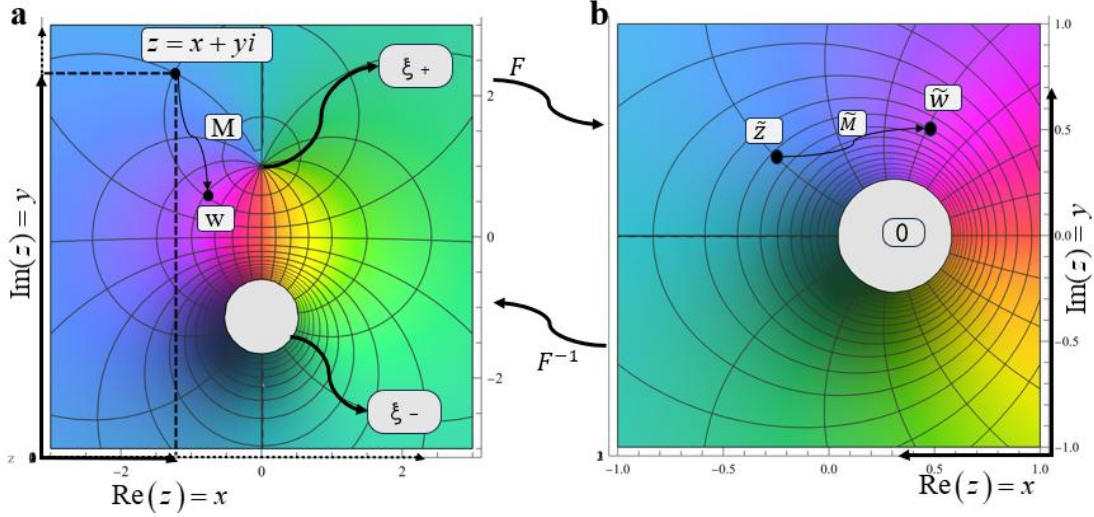


**Fig. 2** Möbius transformation diagram

In the simplest Möbius transformation (see **Fig. 2a**),  $F(z) = \frac{z - \xi_+}{z - \xi_-}$  the transformation maps one fixed point (set to  $\xi_+$ ) to zero and the other fixed point ( $\xi_-$ ) to  $\infty$  infinity. **Fig. 2b** illustrates the image on the left under this Möbius transformation.

#### 2.4 Lorentz transformation

Einstein discovered that there exists a spacetime interval  $\Gamma$  [27] between an observer and an event, such that the values of the spacetime interval seen by two observers are consistent. This spacetime interval  $\Gamma$  is defined by its square:

$$\Gamma^2 = T^2 - (X^2 + Y^2 + Z^2) = \tilde{T}^2 - (\tilde{X}^2 + \tilde{Y}^2 + \tilde{Z}^2) \quad (15)$$

Minkowski realized that this interval was a correct extension of the concept of distance, suitable for use in spacetime. The equidistant transformation and symmetry of spacetime maintain this interval's invariance. However, it is very different from the usual distance: the square of the interval between different events can be zero or even negative.

if two observers focus on the same photon, what they see is consistent, with each event along the photon's trajectory in spacetime having  $\Gamma = 0$ . This four-dimensional



vector, which points to a specific light ray and has its "length" vanish, is called a zero vector.

The Lorentz transformation  $L$  is a linear transformation in spacetime, essentially a  $(4 \times 4)$  matrix that maps an observer's observation  $(T, X, Y, Z)$  of an event to another observer's observation  $(\tilde{T}, \tilde{X}, \tilde{Y}, \tilde{Z})$  of the same event. In other words,  $L$  maintains a constant spatiotemporal distance, and the observations of two observers on the spatiotemporal interval of the same event are consistent.

Imagine an event  $O$  that generates an electric spark, emitting photons that propagate uniformly in all directions, forming a spherical surface centered at the origin. As time progresses, the radius of the spherical surface increases. At the time  $T = 1$ , the photon forms a sphere with a radius of 1, which is now represented by a Riemann sphere. Thus, it can be considered that the sphere composed of these photons consists of points marked with spacetime coordinates  $(1, X, Y, Z)$ , which can also be represented by complex numbers.

The projection formula  $z = (z_1/z_2)$  onto the polar plane of the ball is given by:

$$X = \frac{\varsigma_1 \bar{\varsigma}_2 + \varsigma_2 \bar{\varsigma}_1}{|\varsigma_1|^2 + |\varsigma_2|^2}, Y = \frac{\varsigma_1 \bar{\varsigma}_2 - \varsigma_2 \bar{\varsigma}_1}{i(|\varsigma_1|^2 + |\varsigma_2|^2)}, Z = \frac{|\varsigma_1|^2 - |\varsigma_2|^2}{|\varsigma_1|^2 + |\varsigma_2|^2} \quad (16)$$

However, each beam of light is equivalent to any zero vector in the direction of that beam of light. If we let  $T = 1$ , we can choose a scalar factor  $|\varsigma_1|^2 + |\varsigma_2|^2$  multiplied by the expression, which eliminates the denominator  $(T = |\varsigma_1|^2 + |\varsigma_2|^2)$ . This new zero vector  $(T, X, Y, Z)$  (along the original spatiotemporal direction) can be represented as

$$\begin{aligned} T &= |\varsigma_1|^2 + |\varsigma_2|^2, \\ X &= \varsigma_1 \bar{\varsigma}_2 + \varsigma_2 \bar{\varsigma}_1, \\ Y &= -i(\varsigma_1 \bar{\varsigma}_2 - \varsigma_2 \bar{\varsigma}_1), \\ Z &= |\varsigma_1|^2 - |\varsigma_2|^2 \end{aligned} \quad (17)$$

It is straightforward to convert these formulas into the following form:

$$\begin{pmatrix} T+Z & X+iY \\ X-iY & T-Z \end{pmatrix} = 2 \begin{pmatrix} \varsigma_1 \bar{\varsigma}_1 & \varsigma_1 \bar{\varsigma}_2 \\ \varsigma_2 \bar{\varsigma}_1 & \varsigma_2 \bar{\varsigma}_2 \end{pmatrix} = 2 \begin{pmatrix} \varsigma_1 \\ \varsigma_2 \end{pmatrix} \begin{pmatrix} \bar{\varsigma}_1 & \bar{\varsigma}_2 \end{pmatrix} \quad (18)$$

which simplifies to:

$$\begin{pmatrix} T+Z & X+iY \\ X-iY & T-Z \end{pmatrix} = 2 \begin{pmatrix} \varsigma_1 \\ \varsigma_2 \end{pmatrix} \begin{pmatrix} \varsigma_1 \\ \varsigma_2 \end{pmatrix}^* \quad (19)$$

Here, the symbol “\*” represents conjugate transposition. The spatiotemporal interval can now be succinctly represented as the determinant of this matrix:

$$\Gamma^2 = T^2 - (X^2 + Y^2 + Z^2) = \det \begin{pmatrix} T+Z & X+iY \\ X-iY & T-Z \end{pmatrix} \quad (20)$$

It is evident that this enlarged spatiotemporal vector is still a zero vector, as expected. The complex projection of the spherical polar plane has been utilized to represent the effect of the Möbius transformation  $z \mapsto \tilde{z} = M(z)$  on this beam of light on the complex plane  $\mathbb{C}$ , as follows:

$$\begin{bmatrix} \varsigma_1 \\ \varsigma_2 \end{bmatrix} \mapsto \begin{bmatrix} \tilde{\varsigma}_1 \\ \tilde{\varsigma}_2 \end{bmatrix} = [M] \begin{bmatrix} \varsigma_1 \\ \varsigma_2 \end{bmatrix} \quad (21)$$

This results in a linear transformation of the zero vector generated by the light trajectory:

$$\begin{pmatrix} T+Z & X+iY \\ X-iY & T-Z \end{pmatrix} \mapsto \begin{pmatrix} \tilde{T}+\tilde{Z} & \tilde{X}+i\tilde{Y} \\ \tilde{X}-i\tilde{Y} & \tilde{T}-\tilde{Z} \end{pmatrix} = [M] \begin{pmatrix} T+Z & X+iY \\ X-iY & T-Z \end{pmatrix} [M]^* \quad (22)$$

Finally, imagine that this linear transformation applies to all spatiotemporal vectors (not just zero vectors). Since  $\det[M] = 1 = \det[M]^*$ , it can be concluded that this linear transformation preserves the spatiotemporal interval:

$$\tilde{\Gamma}^2 = \det \left\{ [M] \begin{pmatrix} T+Z & X+iY \\ X-iY & T-Z \end{pmatrix} [M]^* \right\} = \Gamma^2 \quad (23)$$

Each Möbius transformation on a complex plane  $\mathbb{C}$  corresponds to a unique Lorentz transformation in spacetime. Conversely, it can be proven that each Lorentz

transformation corresponds to a unique Möbius transformation. Therefore, there exists a one-to-one correspondence between the Möbius transformation and the Lorentz transform, which reflects the invariance of spatiotemporal geometry in different reference frames.

### 2.5 Fluctuation of electron mass

The electron and positron can interact by exchanging a photon, and the photon can, in turn, transform into an electron-positron[28] pair. as shown in **Fig. 3**, the shaded region represents the vacuum polarization tensor, denoted as  $i\Pi_{\mu\nu}(q)$ . Based on infinitely many Feynman diagrams, as illustrated in **Fig. 4**, an approximation using the lowest-order diagram in **Fig. 3** with the vacuum polarization tensor leads to the diagram shown in **Fig. 5**.

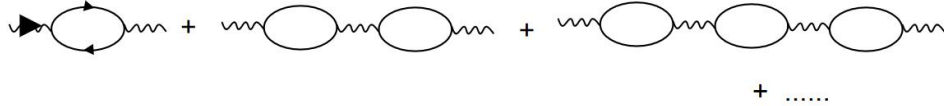


**Fig. 3** the process of mutual annihilation

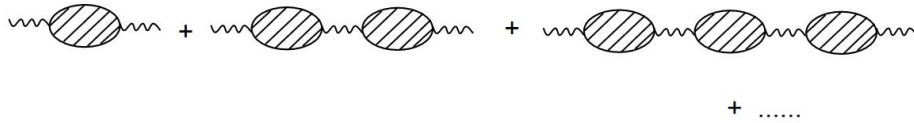


**Fig. 4** physical photon propagation

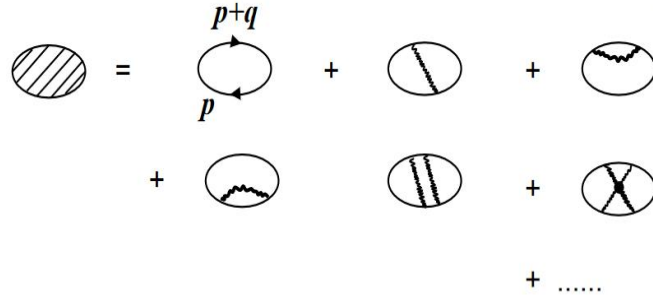


**Fig. 5** infinite Feynman diagrams

The Lagrangian for this transformation  $A \rightarrow (1/e)A$  is given by:

$$L = \bar{\psi} \left[ i\gamma^\mu (\partial_\mu - iA_\mu) - m \right] \psi - \frac{1}{4e^2} F_{\mu\nu} F^{\mu\nu} \quad (24)$$

At  $\psi \rightarrow e^{i\alpha}\psi, A_\mu \rightarrow A_\mu + \partial_\mu\alpha$  this point, the photon propagator taking the inverse of

$\frac{1}{4e^2} F_{\mu\nu} F^{\mu\nu}$  is proportional to  $e^2$  :

$$iD_{\mu\nu}(q) = \frac{-ie^2}{q^2} \left( g_{\mu\nu} - (1-\xi) \frac{q_\mu q_\nu}{q^2} \right) \quad (25)$$

According to the combination of gauge -invariant diagrams and Lorentz invariance:

$$\begin{cases} q_\mu \Pi_{\mu\nu}(q) = 0 \\ \Pi_{\mu\nu}(q) = (q_\mu q_\nu - g_{\mu\nu} q^2) \Pi(q^2) \end{cases} \quad (26)$$

The physical photon propagation in **Fig. 4** is represented by the following geometric series:

$$\begin{aligned} iD_{\mu\nu}^P(q) &= iD_{\mu\nu}(q) + iD_{\mu\lambda}(q) i\Pi^{\lambda\rho}(q) iD_{\rho\nu}(q) \\ &\quad + iD_{\mu\lambda}(q) i\Pi^{\lambda\rho}(q) iD_{\rho\sigma}(q) i\Pi^{\sigma\kappa}(q) iD_{\kappa\nu}(q) + \dots \\ &= \frac{-ie^2}{q^2} g_{\mu\nu} \frac{1}{1+e^2 \Pi(q^2)} + q_\mu q_\nu \end{aligned} \quad (27)$$

$(1-\xi) \frac{q_\mu q_\nu}{q^2}$  in part  $iD_{\mu\nu}(q) = \frac{-ie^2}{q^2} \left( g_{\mu\nu} - (1-\xi) \frac{q_\mu q_\nu}{q^2} \right)$  encounters  $\Pi_{\lambda\rho}(q)$  as 0, in **Eq. 27**,

and the parameter  $\xi$  appears only in the  $q_\mu q_\nu$  term and not in the physical amplitude, in **Eq. 26**.

The residue of the pole  $iD_{\mu\nu}^P(q)$  is the square of the heavy positive charge, also known as physics:

$$e_R^2 = e^2 \frac{1}{1+e^2 \Pi(0)} \quad (28)$$

Using Pauli-Villas regularization and integral convergence, we obtain:

$$i\Pi^{\mu\nu}(q) = (-) \int \frac{d^4 p}{(2\pi)^4} \frac{N_{\mu\nu}}{D} \quad (29)$$

Inside

$$N_{\mu\nu} = \text{tr} \left[ \gamma_\nu (p+q+m) \gamma_\mu (p+m) \right]$$

(30)

$$\frac{1}{D} = \int_0^1 d\alpha \frac{1}{D}$$

(31)

Inside

$$\begin{cases} D = [l^2 + \alpha(1+\alpha)q^2 - m^2 + i\varepsilon]^2 \\ l = p + \alpha q \end{cases}$$

(32)

Finally, you can get:

$$\begin{aligned} \Pi_{\mu\nu}(q) = & -\frac{1}{2\pi^2} (q_\mu q_\nu - g_{\mu\nu} q^2) \int_0^1 d\alpha (1-\alpha) \\ & \cdot \left\{ \ln[m^2 - \alpha(1-\alpha)q^2] - \ln[m_\alpha^2 - \alpha(1-\alpha)q^2] \right\} \end{aligned}$$

(33)

We define:

$$\ln M^2 = \ln m_\alpha^2$$

(34)

Then:

$$\Pi(q^2) = \frac{1}{2\pi^2} \int_0^1 d\alpha (1-\alpha) \ln \frac{M^2}{m^2 - \alpha(1-\alpha)q^2}$$

(35)

Summarizing **Eq. (28)** and **(35)**:

$$e_R^2 = e^2 \frac{1}{1 + \left[ \frac{e^2}{12\pi^2} \right] \ln \left( \frac{M^2}{m^2} \right)} \simeq e^2 \left( 1 - \frac{e^2}{12\pi^2} \ln \frac{M^2}{m^2} \right)$$

(36)

While  $M^2$  representing the parameter of the ignorance bound, which confirms that the magnitude of the fluctuation mass of the charge is related to the imaginary mass  $M$ .

$$\Delta e^2 = \frac{e^2}{12\pi^2} \ln \frac{M^2}{m^2}$$

(37)

## 2.6 Principles of tropical geometry

Tropical geometry is a variant of algebraic geometry based on "Tropical

Mathematics ."In tropical geometry, the basic research object is the tropical semiring  $(\mathbb{R} \cup \{\infty\}, \oplus, \odot)$  [29], and traditional operations such as addition and multiplication are replaced by "tropical addition" and "tropical multiplication":

$$x \oplus y = \min(x, y), \quad x \odot y = x + y \tag{38}$$

The curve defined by a polynomial equation is referred to as an algebraic curve. In traditional algebraic geometry, algebraic curves are described by solving equations; In tropical geometry, these curves are transformed into objects related to 'tropical addition' and 'tropical multiplication,' known as planar tropical curves. For polynomials with two variables:

$$p(x, y) = \bigoplus_{(i,j)} c_{ij} \odot x^i \odot y^j \tag{39}$$

The corresponding planar tropical curve  $V(p)$  is the set of all points  $(x, y)$  satisfying this transformation. If  $p$  is a quadratic polynomial:

$p(x, y) = 1 \odot x^2 \oplus 1 \odot y^2 \oplus 2 \odot xy$  the corresponding tropical curve  $V(p)$  forms a triangle with vertices at  $(0,0)$ ,  $(0,2)$ ,  $(2,0)$ :

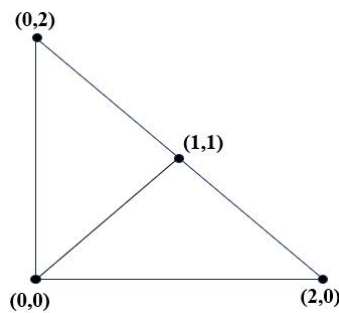


**Fig. 6** Tropical geometry  $V(1 \odot x^2 \oplus 1 \odot y^2 \oplus 2 \odot xy)$

A tropical matrix refers to a matrix whose elements are defined using tropical addition and multiplication operations. Unlike matrix operations in traditional linear algebra, tropical matrices adhere to the rules of tropical mathematics. When discussing eigenvalues of tropical matrices, the concept is analogous to eigenvalues in classical linear algebra but operates under tropical rules. Specifically, each quadratic polynomial can be associated with a  $(2 \times 2)$  tropical matrix. For example, a

polynomial  $f(x,y)=2xy$  corresponds to a tropical matrix  $A=\begin{bmatrix} 0 & 1 \\ 1 & 0 \end{bmatrix}$ , see the Supporting Materials. Similarly, for other forms of polynomials, such as  $f(x,y)=x^2+y^2+2xy$  or  $f(x,y)=x^2+y^2$ , they can also be associated with tropical matrices(Matrix of Quadratic Form)  $A=\begin{bmatrix} 1 & 1 \\ 1 & 1 \end{bmatrix}$  and  $A=\begin{bmatrix} 1 & 0 \\ 0 & 1 \end{bmatrix}$ , respectively. Under this framework, tropical gradient maps can be constructed, showing the relationships and transformation rules between different polynomials and their corresponding tropical matrices:

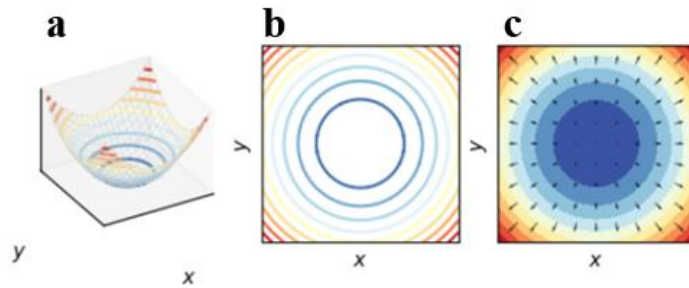


**Fig. 7** Tropical geometry diagram

In **Fig. 7**, **a** presents the 3D surface plot of the quadratic polynomial, **b** shows the 2D contour plot of its function values, and **c** overlays the gradient field vectors on the 2D contour plot. This graph not only provides an intuitive visualization tool for understanding the structure of tropical matrices but also reveals the profound connection between polynomials and matrices in tropical algebra. Tropical geometry represents the equivalent mass in Schrödinger's equation. Lorentz transformation

In quantum mechanics, reduced mass is a parameter that describes the "effective" inertia exhibited by particles in certain systems[30]. Assuming we introduce the reduced mass effect in Schrödinger's equation, the reduced mass typically affects the energy spectrum of particles, especially in strong electric fields or non-uniform media. The definition of reduced mass  $\bar{M}$  is closely related to the relationship between potential energy and kinetic energy terms in the wave equation. The Hamiltonian operator is:

$$\hat{H} = -\frac{\hbar^2}{2m} \nabla^2 + U(\vec{r}) \quad (40)$$

The kinetic energy operator is  $\hat{E}_k = -\frac{\hbar^2}{2m} \nabla^2$ , where  $\nabla^2 = \frac{\partial^2}{\partial x^2} + \frac{\partial^2}{\partial y^2} + \frac{\partial^2}{\partial z^2}$  is the

Laplace operator. For the kinetic energy operator, multiply both sides by  $\frac{1}{2}x^2$ :

$$\frac{1}{2}\hat{E}_k x^2 = -\frac{\hbar^2}{2m}\nabla^2\left(\frac{1}{2}x^2\right) = -\frac{\hbar^2}{2m} \quad (41)$$

therefore:

$$\frac{1}{2}\hat{E}_k x_1^2 = -\frac{\hbar^2}{2m_1}, \quad \frac{1}{2}\hat{E}_k x_2^2 = -\frac{\hbar^2}{2m_2} \quad (42)$$

let  $x_1 = x, x_2 = y$ , so we have:

$$\frac{1}{2}(\hat{E}_k x^2 + \hat{E}_k y^2) = -\frac{\hbar^2}{2m_x} - \frac{\hbar^2}{2m_y} = -\frac{\hbar^2}{2}\left(\frac{1}{m_x} + \frac{1}{m_y}\right) = -\frac{\hbar^2}{2}\left(\frac{m_x + m_y}{m_x m_y}\right) \quad (43)$$

further,

$$\hat{E}_k x^2 + \hat{E}_k y^2 = -\hbar^2\left(\frac{m_x + m_y}{m_x m_y}\right) = -\hbar^2\bar{M} \quad (44)$$

among them,  $\bar{M}$  is the equivalent mass,  $\hat{E}_k$  is the kinetic energy operator, and  $\hbar$  is the Planck constant. In this form, the reduced mass  $\bar{M}$  can be seen as a transformation result generated according to the rules of tropical geometry, representing how the effective mass of particles varies with the state of the system under different conditions. **Eq.43** satisfies the Lorentz transformation, see the Supporting Material.

Therefore,  $-\hbar^2\bar{M}$  can be represented in tropical geometry by the following formula:

$$f(x, y) = \hat{E}_k x^2 + \hat{E}_k y^2 \quad (45)$$

the corresponding tropical matrix is:

$$A = \begin{bmatrix} E_k & 0 \\ 0 & E_k \end{bmatrix} \quad (46)$$

When combining tropical geometry with the equivalent mass equation in



Schrödinger's equation, we propose a way to re-characterize the equivalent mass through tropical operations. By representing the converted mass and potential energy terms as tropical polynomials, we can not only capture nonlinear effects in the system but also provide a new mathematical tool for complex systems in quantum mechanics. Future research can further explore the application of tropical geometry in other physical models, especially in dealing with non-uniform and nonlinear quantum systems.

### **3.Results and discussion**

#### **3.1 Geometric structures**

The two-dimensional bilayer  $\text{MX}_2$  exhibits a typical layered structure, where M atoms and X atoms form a hexagonal arrangement through covalent bonds, and the two layers interact with each other through weak van der Waals forces. Geometric optimization was performed on the initial structures of the two-dimensional bilayer  $\text{WS}_2$ ,  $\text{WSe}_2$ ,  $\text{WTe}_2$ , and heterojunctions  $\text{MoS}_2/\text{WSe}_2$ ,  $\text{MoS}_2/\text{MoTe}_2$ , and  $\text{WSe}_2/\text{MoTe}_2$ . The optimized results are shown in **Fig. 8**. For different combinations of M (Mo, W) and X (S, Se, Te), variations in atomic radius and electronegativity can lead to variations in lattice constants and interlayer distances. The interlayer distances of  $\text{MoS}_2/\text{WSe}_2$ ,  $\text{MoS}_2/\text{MoTe}_2$ ,  $\text{WSe}_2/\text{MoTe}_2$ ,  $\text{WS}_2$ ,  $\text{WSe}_2$  and  $\text{WTe}_2$  were found to be 3.837, 3.918, 3.895, 3.672, 3.740 and 3.900 Å. The changes in bond length and bond angle reflect the variations in the strength and geometric configuration of chemical bonds. Generally, the shorter the bond length, the stronger the chemical bond. From the calculation results, it can be seen that as the radius of X atom increases, the M-X bond length gradually increases, which is due to the increase in atomic size leading to an increase in interatomic distance. Although The change in bond angle is relatively small, it does exhibit certain patterns, which are related to the symmetry of the crystal structure and the interactions between atoms.

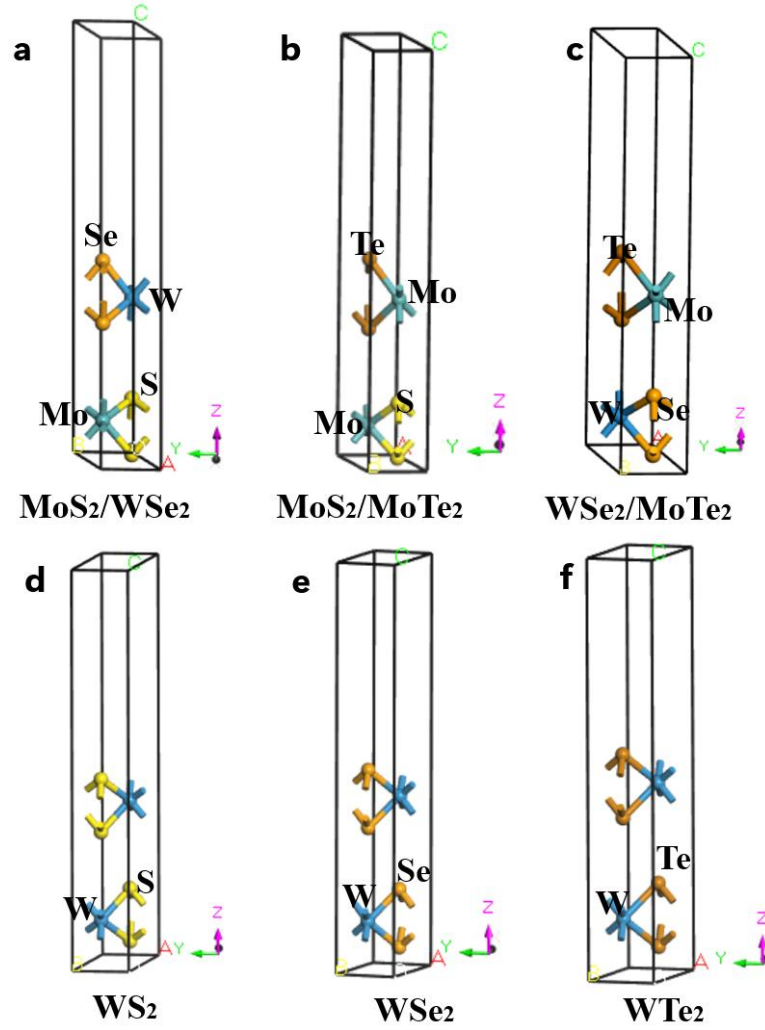


**Fig. 8** Geometrical structures of (a) MoS<sub>2</sub>/WSe<sub>2</sub>, (b) MoS<sub>2</sub>/MoTe<sub>2</sub>, (c) WSe<sub>2</sub>/MoTe<sub>2</sub>, (d) WS<sub>2</sub>, (e) WSe<sub>2</sub> and (f) WTe<sub>2</sub> and the lattice structure parameter sets are listed in **Table 2**.

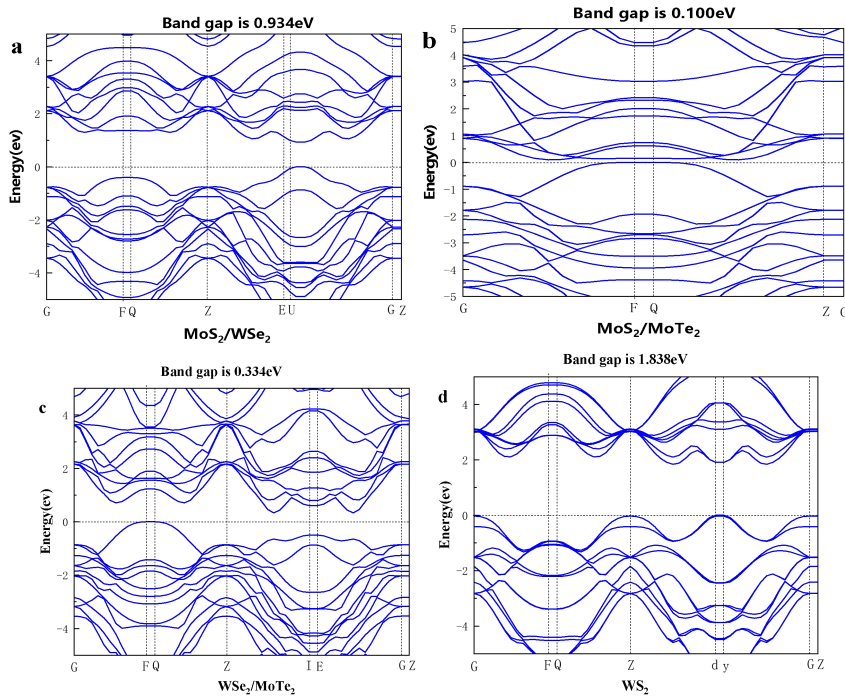
**Table 2** Lattice and structural parameters of two-dimensional bilayer MX<sub>2</sub>

	Interlayer distance (Å)	Lattice parameters (° / Å)						Bond length (Å)	Bond angle (Å)
		$\alpha$	$\beta$	$\gamma$	a	b	c		
MoS <sub>2</sub> /WSe <sub>2</sub>	3.837	90	90	120	3.160	3.160	24.000	(Mo-S)	(S-Mo-S)
								2.408	81.425
MoS <sub>2</sub> /MoTe <sub>2</sub>	3.918	90	90	60	3.160	3.160	24.000	(W-Se)	(Se-W-Se)
								2.522	87.389
WSe <sub>2</sub> /MoTe <sub>2</sub>	3.895	90	90	60	3.282	3.282	24.000	(Mo-S)	(S-Mo-S)
								2.408	81.432
WS <sub>2</sub>								(Mo-Te)	(Te-Mo-Te)
								2.699	94.948
WSe <sub>2</sub>								(W-Se)	(Se-W-Se)
								2.542	83.587
WTe <sub>2</sub>								(Mo-Te)	(Te-Mo-Te)
								2.704	91.119

WS <sub>2</sub>	3.672	90	90	120	3.153	3.153	24.000	2.413	82.069
WSe <sub>2</sub>	3.740	90	90	120	3.282	3.282	24.000	2.542	83.588
WTe <sub>2</sub>	3.900	90	90	120	3.600	3.600	24.000	2.752	81.963

### 3.2 Band structure, local density of states (LDOS), deformation charge density, and electronic properties

The band structure of the two-dimensional bilayer MX<sub>2</sub> calculated using DFT is shown in **Fig. 9**. It can be observed that all compounds exhibit semiconductor properties, with bandgap widths varying within a certain range. Molecular dynamics simulation shows that the two-dimensional bilayer MX<sub>2</sub> is stable. The results are shown in the supplemental material. The bandgap width of MoS<sub>2</sub>/WSe<sub>2</sub> is 0.934 eV, MoS<sub>2</sub>/MoTe<sub>2</sub> is 0.100 eV, WSe<sub>2</sub>/MoTe<sub>2</sub> is 0.334 eV, WS<sub>2</sub> is 1.838 eV, WSe<sub>2</sub> is 1.496 eV, and WTe<sub>2</sub> is 0.917 eV, respectively. From the shape of the band structure, the energy bands near the top of the valence band and the bottom of the conduction band exhibit different dispersion relations, reflecting the differences in the effective mass and motion characteristics of electrons in different directions.



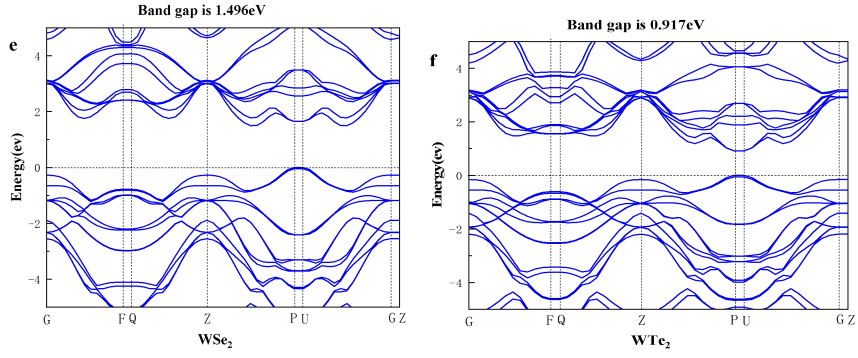


**Fig. 9** Band structure of (a) MoS<sub>2</sub>/WSe<sub>2</sub>, (b) MoS<sub>2</sub>/MoTe<sub>2</sub>, (c) WSe<sub>2</sub>/MoTe<sub>2</sub>, (d) WS<sub>2</sub>, (e) WSe<sub>2</sub> and (f) WTe<sub>2</sub>.

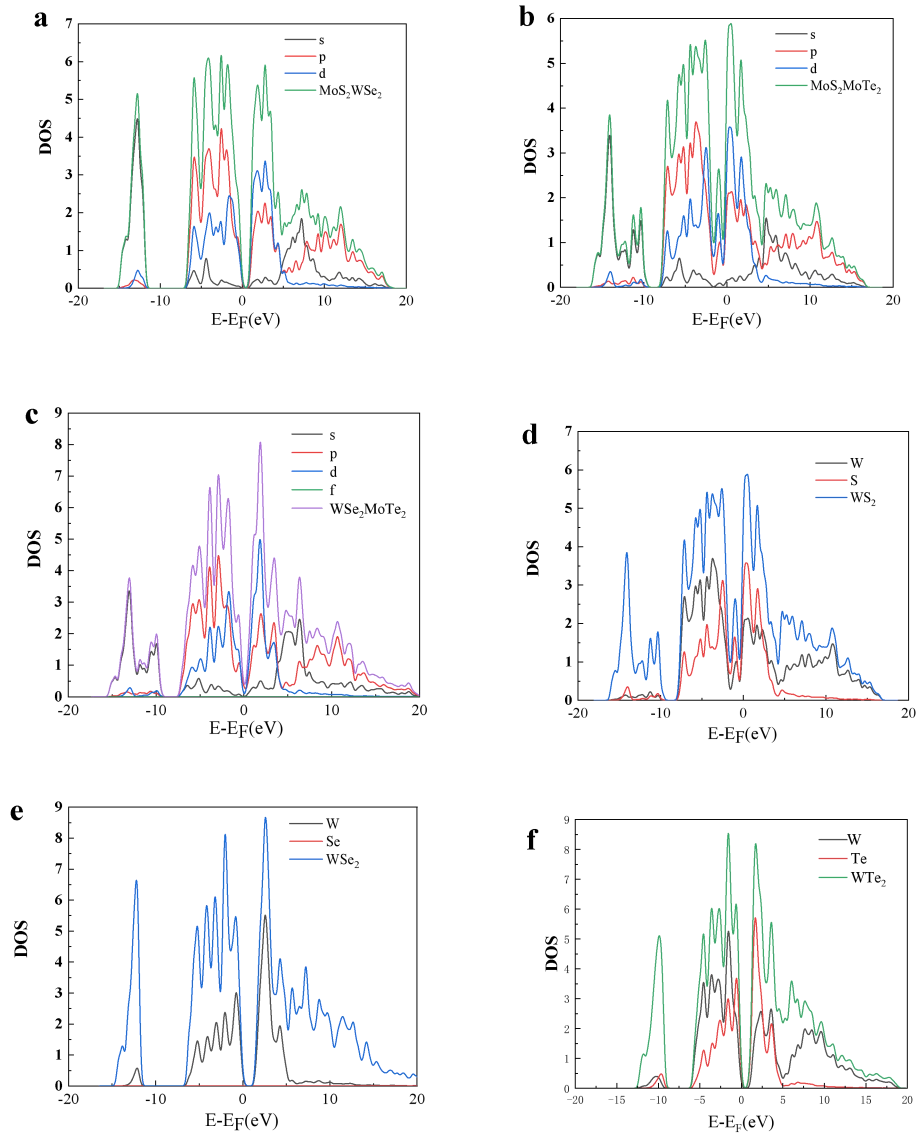


**Fig. 10** density of states (DOS) of (a) MoS<sub>2</sub>/WSe<sub>2</sub>, (b) MoS<sub>2</sub>/MoTe<sub>2</sub>, (c) WSe<sub>2</sub>/MoTe<sub>2</sub>, (d) WS<sub>2</sub>, (e) WSe<sub>2</sub> and (f) WTe<sub>2</sub>

**Fig. 10** shows the total DOS and PDOS of the two-dimensional bilayer MX<sub>2</sub>.

From the total DOS, it can be seen that the main peaks of electron density distribution in the conductive band of MoS<sub>2</sub>/WSe<sub>2</sub> heterojunction, MoS<sub>2</sub>/MoTe<sub>2</sub> heterojunction, and WSe<sub>2</sub>/MoTe<sub>2</sub> heterojunction are all in the negative energy direction, indicating that the structure is relatively stable. Near the Fermi level, the DOS is mainly contributed by the d orbitals of M and the p-orbitals of X. For Mo-based compounds, the d orbitals of Mo make a significant contribution in the lower energy region, while the p-orbitals of X are relatively prominent in the higher energy region. For W-based compounds, similar orbital contribution characteristics also exist, but due to the different atomic structure and electronic properties of W compared to Mo, the specific distribution of DOS varies. The DOS further reveals the details of the contribution of different atomic orbitals to electronic states, as well as their mutual hybridization. For example, in MoS<sub>2</sub>, the d<sub>x<sup>2</sup>-y<sup>2</sup></sub> and d<sub>z</sub> orbitals of Mo have strong hybridization with the p<sub>x</sub> and p<sub>y</sub> orbitals of S within a certain energy range. This orbital hybridization has a significant impact on the formation of chemical bonds and the stability of electronic structures. The energy levels of two-dimensional bilayer WSe<sub>2</sub>, WS<sub>2</sub>, and WTe<sub>2</sub> intersect with one or more energy bands, indicating a high electron mobility. Therefore, these six types can be used as alternative materials for preparing electronic devices.

To analyze the electronic properties of the bonds, we used the deformation charge density (**Fig. 7**) of the Mo-S chemical bonds in MoS<sub>2</sub>/WSe<sub>2</sub> (**Fig. 7a**)、 the Mo-Te chemical bonds in MoS<sub>2</sub>/MoTe<sub>2</sub> (**Fig. 7b**)、 the W-Se chemical bonds in WSe<sub>2</sub>/MoTe<sub>2</sub>(**Fig. 7c**)、 the W-S chemical bonds in WS<sub>2</sub> **Fig. 7d**)、 the W-Se chemical bonds in WSe<sub>2</sub>(**Fig. 7e**) and the W-Te chemical bonds in WTe<sub>2</sub> (**Fig. 7f**). The electron distributions are indicated by the color scale, where the blue and red areas represent an increase and decrease, respectively, in the number of electrons. The metal atoms of Te, S and Se is mainly displayed in blue, indicating a positive deformation charge density and the accumulation of a large amount of charge in this region of the structure. The W and Mo atoms are mainly displayed in red, indicating a negative deformation charge density and a large amount of charge divergence. It can be seen that the amount of charge transfer varies with the change of the X atom, which is related to the electronegativity of the X atom. X atoms with higher electronegativity attract more electrons, resulting in an increase in charge transfer. Meanwhile, due to its higher electronegativity, W atoms have a relatively smaller charge transfer amount

compared to Mo atoms when combined with the same X atom.

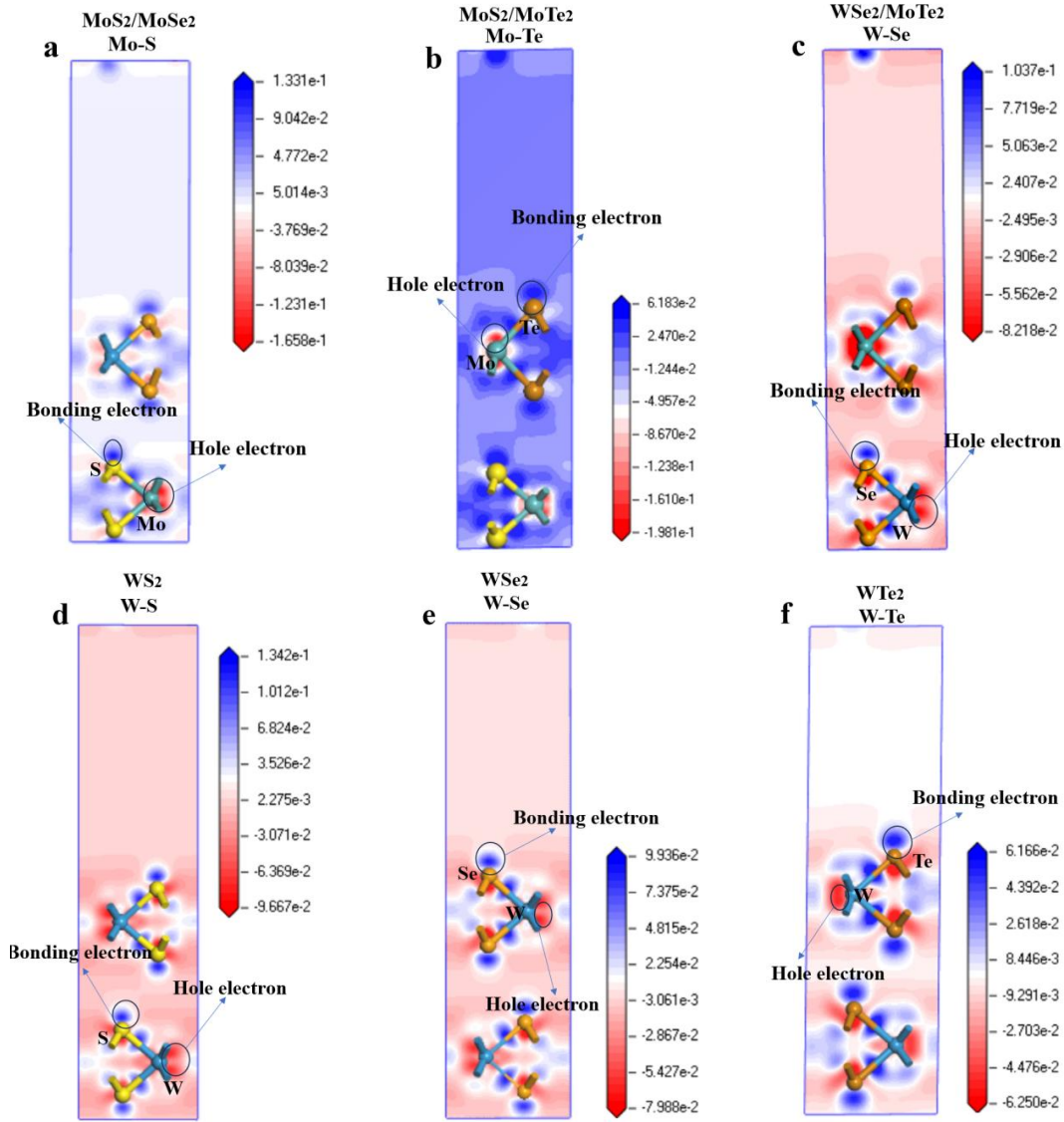


**Fig. 11** Deformation charge densities of (a) MoS<sub>2</sub>/WSe<sub>2</sub>, (b) MoS<sub>2</sub>/MoTe<sub>2</sub>, (c) WSe<sub>2</sub>/MoTe<sub>2</sub>, (d) WS<sub>2</sub>, (e) WSe<sub>2</sub> and (f) WTe<sub>2</sub>

The established BBC model was used to convert the Hamiltonian values into bonding values (Table 3).

**Table 3** Deformation charge density  $\delta\rho(\vec{r}_{ij})$  and deformation bond energy

$\delta V_{bc}(\vec{r}_{ij})$ , as obtained from the BBC model

$$\left( \varepsilon_0 = 8.85 \times 10^{-12} \text{ C}^2 \text{ N}^{-1} \text{ m}^{-2}, e = 1.60 \times 10^{-19} \text{ C}, |\vec{r}_{ij}| \approx d_{ij} / 2 \right)$$

	MoS <sub>2</sub> / WSe <sub>2</sub>	MoS <sub>2</sub> / MoTe <sub>2</sub>	WSe <sub>2</sub> / MoTe <sub>2</sub>	WS <sub>2</sub>	WSe <sub>2</sub>	WTe <sub>2</sub>
$r_{ij}$ ( Å )	1.20	1.35	1.27	1.21	1.27	1.38
	Mo-S	Mo-Te	W-Se	W-S	W-Se	W-Te

$r_i$ ( Å )	1.05 (S)	1.38 (Te)	1.20 (Se)	1.05 (S)	1.20 (Se)	1.38 (Te)
$\vec{r}_j$ ( Å )	1.54 (Mo)	1.54 (Mo)	1.62 (W)	1.62 (W)	1.62 (W)	1.62 (W)
$\delta\rho^{Bonding-electron}(\vec{r}_i)\left(\frac{e}{\text{Å}^3}\right)$	0.1331 (S)	0.0618 (Te)	0.1038 (Se)	0.1342 (S)	0.0994 (Se)	0.0676 (Te)
$\delta\rho^{Hole-electron}(\vec{r}_j)\left(\frac{e}{\text{Å}^3}\right)$	-0.1658 (Mo)	-0.1981 (Mo)	-0.0822 (W)	-0.0967 (W)	-0.0799 (W)	-0.0600 (W)
$\delta V_{bc}^{bonding}(\vec{r}_{ij})$ (eV)	-0.5590	-0.6258	-0.3549	-0.3795	-0.3303	-0.2361
$\delta V_{bc}^{Antibonding}(\vec{r}_i)$ (eV)	0.1626 (S)	0.1374 (Te)	0.1928 (Se)	0.1653 (S)	0.1768 (Se)	0.1644 (Te)
$\delta V_{bc}^{Antibonding}(\vec{r}_j)$ (eV)	1.7120 (Mo)	2.444 (Mo)	0.5421 (W)	0.7502 (W)	0.5122 (W)	0.2888 (W)

The deformation charge density and electronic radius were used to calculate the deformation bond energies from **Eq. 7** as follows: -0.5590, -0.6258, -0.3549, -0.3795, -0.3303 and -0.2361 eV for Mo-S in MoS<sub>2</sub>/WSe<sub>2</sub>, Mo-Te in MoS<sub>2</sub>/MoTe<sub>2</sub>, W-Se in WSe<sub>2</sub>/MoTe<sub>2</sub>, W-S in WS<sub>2</sub>, W-Se in WSe<sub>2</sub> and W-Te in WTe<sub>2</sub>, respectively.

### 3.3 Non-Hermitian bonding of MoS<sub>2</sub>/MoSe<sub>2</sub>、 MoS<sub>2</sub>/MoTe<sub>2</sub>、 WSe<sub>2</sub>/Mo-Te、 WS<sub>2</sub>、 WSe<sub>2</sub> and WTe<sub>2</sub>

$$M(z) = \frac{az+b}{cz+d} \rightarrow [M] = \begin{bmatrix} a & b \\ c & d \end{bmatrix} \quad (48)$$

The Möbius transform is a fractional linear function that maps point  $z$  on a complex plane to a unique point, where  $a$ ,  $b$ ,  $c$ , and  $d$  are plurals, and  $ad - bc \neq 0$ . To use **Eq. 11** for a point  $W = (X, Y, Z)$  in real space, we first normalize the coordinates

$R_1(x_1, y_1, z_1)$  and  $R_2(x_2, y_2, z_2)$  of two atoms in real space. The distance  $l$  between them is:

$$\sqrt{(x_1 - x_2)^2 + (y_1 - y_2)^2 + (z_1 - z_2)^2} = l \quad (49)$$

Therefore:

$$\sqrt{\frac{(x_1 - x_2)^2}{l^2} + \frac{(y_1 - y_2)^2}{l^2} + \frac{(z_1 - z_2)^2}{l^2}} = 1 \quad (50)$$

Order:

$$\begin{cases} X = \frac{x_1 - x_2}{l} \\ Y = \frac{y_1 - y_2}{l} \\ Z = \frac{z_1 - z_2}{l} \end{cases} \quad (51)$$

Point  $W = (X, Y, Z)$  in real space satisfies  $\sqrt{X^2 + Y^2 + Z^2} = 1$ .

For a point  $w$  in the complex number set  $C$ ,  $w = x + iy$ ,  $\text{Re}(w) = x$ , and  $\text{Im}(w) = y$ .

As the projection point of  $W$ ,  $w$  satisfies  $x = \frac{X}{1-Z}$  or  $y = \frac{Y}{1-Z}$ . The projections of the atomic coordinates from real space onto a two-dimensional complex plane are listed in **Table 4**.

**Table 4** Spatial coordinates of chemical bonds between MoS<sub>2</sub>/WSe<sub>2</sub>, MoS<sub>2</sub>/MoTe<sub>2</sub>, WSe<sub>2</sub>/MoTe<sub>2</sub>, WS<sub>2</sub>, WSe<sub>2</sub> and WTe<sub>2</sub> and their projection points on the complex plane.

	Atom 1 (coordinates)	Atom 2 (coordinates)	X	Y	Z	W
MoS <sub>2</sub> /WSe <sub>2</sub>	Mo (0.91,1.58,2.08)	S (1.82,0,3.65)	0.1430	0.4312	0.4258	0.2491+0.7509i
MoS <sub>2</sub> /MoTe <sub>2</sub>	Mo (0.91,1.58,9.51)	Te (1.82,3.16,11.50)	0.1137	0.3427	0.5436	0.2491+0.7509i
WSe <sub>2</sub> /MoTe <sub>2</sub>	W (1.91,3.30,2.22)	Se (0.96,1.65,3.91)	0.1393	0.4201	0.4407	0.2490+0.7510i
WS <sub>2</sub>	W (1.82,0,9.58)	S (0.91,1.58,11,17)	0.1415	0.4265	0.4320	0.2491+0.7509i
WSe <sub>2</sub>	W (1.90,0,10.04)	Se (0.95,1.63,11.74)	0.1399	0.4120	0.4481	0.2536+0.7464i
WTe <sub>2</sub>	W (2.08,0,10.85)	Te (1.04,1.80,12.65)	0.1430	0.4268	0.4285	0.2503+0.7497i

Based on **Eq. 49**, the projection points of Mo-S in MoS<sub>2</sub>/WSe<sub>2</sub>, Mo-Te in MoS<sub>2</sub>/MoTe<sub>2</sub>, W-Se in WSe<sub>2</sub>/MoTe<sub>2</sub>, W-S in WS<sub>2</sub>, W-Se in WSe<sub>2</sub> and W-Te in WTe<sub>2</sub> in a two-dimensional complex plane are  $0.2491 + 0.7509i$ ,  $0.2491 + 0.7509i$ ,  $0.2490 + 0.7510i$ ,  $0.2491 + 0.7509i$ ,  $0.2436 + 0.7464i$  and  $0.2503 + 0.7497i$ , respectively.

The elements of the matrix  $\begin{bmatrix} a & b \\ c & d \end{bmatrix}$  in the Möbius transformation are complex



numbers. To determine the projection of chemical bond energy, according to **Table 4**, we define the bond energy coefficients  $V_{11}$ ,  $V_{22}$ , and  $V_{12}$  as:

$$\begin{cases} V_{11} = \frac{1}{4\pi\epsilon_0} \frac{e^2}{2|\vec{r}_i|} \int d^3r \int d^3r \delta\rho^{Bonding-electron}(\vec{r}_i) \delta\rho^{Bonding-electron}(\vec{r}_i) = \delta V_{bc}^{Antibonding}(\vec{r}_i) \\ V_{22} = \frac{1}{4\pi\epsilon_0} \frac{e^2}{2|\vec{r}_j|} \int d^3r \int d^3r \delta\rho^{Hole-electron}(\vec{r}_j) \delta\rho^{Hole-electron}(\vec{r}_j) = \delta V_{bc}^{Antibonding}(\vec{r}_j) \\ V_{12} = \frac{1}{4\pi\epsilon_0} \frac{e^2}{2|\vec{r}_i - \vec{r}_j|} \int d^3r \int d^3r \delta\rho^{Bonding-electron}(\vec{r}_{ij}) \delta\rho^{Hole-electron}(\vec{r}_{ij}) = \delta V_{bc}^{bonding}(\vec{r}_{ij}) \end{cases} \quad (52)$$

Substituting **Eq. 49** and  $Z=w=x+iy$  into the matrix elements of the Möbius transformation yields:

$$\begin{bmatrix} a & b \\ c & d \end{bmatrix} = \begin{bmatrix} V_{12}i & V_{11}i \\ V_{21}i & V_{22}i \end{bmatrix} \quad (53)$$

Substituting **Eq. 50** into **Eq. 48**, we obtain:

$$a = c = V_{12} = V_{21} = \delta V_{bc}^{bonding}(\vec{r}_{ij}), b = V_{11} = \delta V_{bc}^{Antibonding}(\vec{r}_i), d = V_{22} = \delta V_{bc}^{Antibonding}(\vec{r}_j) \quad (54)$$

Substituting **Eq. 51** into **Eq. 48** yields the Tan and Bo transformation[31] with the chemical bond energy as a coefficient:

$$F(z) = \frac{V_{12}iZ + V_{11}i}{V_{21}iZ + V_{22}i} \quad (55)$$

The chemical bond energy as a coefficient is used to determine the eigenvalues of the Hamiltonian energy, which are transformed into energy projections in the complex space through the Möbius transformation. The chemical bond energy coefficients are calculated by substituting **Eq. 49** into **Eq. 52** is substituted into **Eq. 55** to obtain the Möbius transformation of MoS<sub>2</sub>/WSe<sub>2</sub>, MoS<sub>2</sub>/MoTe<sub>2</sub>, WSe<sub>2</sub>/MoTe<sub>2</sub>, WS<sub>2</sub>, WSe<sub>2</sub> and WTe<sub>2</sub>.

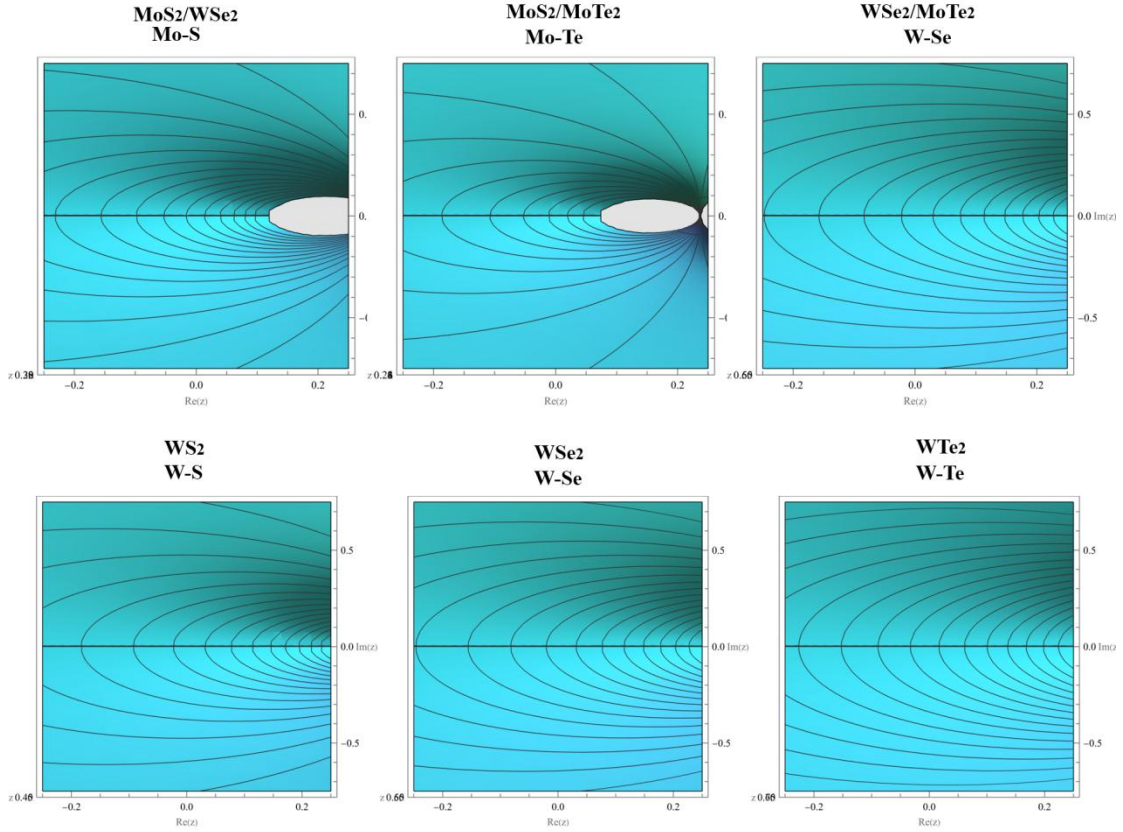


**Fig. 12** Non-Hermitian chemical bond of MoS<sub>2</sub>/WSe<sub>2</sub>, MoS<sub>2</sub>/MoTe<sub>2</sub>, WSe<sub>2</sub>/MoTe<sub>2</sub>, WS<sub>2</sub>, WSe<sub>2</sub> and WTe<sub>2</sub>

The calculations using the  $Z=w=x+iy$  function, illustrated in **Fig.12**, are as follows:

$$F(z) = \frac{-0.5590i \cdot w + 0.1626i}{-0.5590i \cdot w + 1.7120i}, \quad w = 0.25 + 0.75i \text{ of Mo-S in MoS}_2/\text{WSe}_2;$$

$$F(z) = \frac{-0.6258i \cdot w + 0.1374i}{-0.6258i \cdot w + 2.4440i}, \quad w = 0.25 + 0.75i \text{ of Mo-Te in MoS}_2/\text{MoTe}_2;$$

$$F(z) = \frac{-0.3549i \cdot w + 0.1928i}{-0.3549i \cdot w + 0.5421i}, \quad w = 0.25 + 0.75i \text{ of W-Se in WSe}_2/\text{MoTe}_2;$$

$$F(z) = \frac{-0.3795i \cdot w + 0.1653i}{-0.3795i \cdot w + 0.7502i}, \quad w = 0.25 + 0.75i \text{ of W-S in WS}_2;$$

$$F(z) = \frac{-0.3303i \cdot w + 0.1768i}{-0.3303i \cdot w + 0.5122i}, \quad w = 0.25 + 0.75i \text{ of W-Se in WSe}_2;$$

$$F(z) = \frac{-0.2361i \cdot w + 0.1644i}{-0.2361i \cdot w + 0.2888i}, \quad w = 0.25 + 0.75i \text{ of W-Te in WTe}_2.$$

### 3.4 Conformal transformation

Each  $R(x+yi)$  can be represented in the following form:

$$R(x+yi) = P(x+yi)/Q(x+yi)$$

(56)

and

$$R(x + yi) = X + Yi,$$

$$R(x - yi) = X - Yi$$

$$(A + Bi)/(C + Di) = (A + Bi)(C - Di)/(C + Di)(C - Di) = \frac{AC + BD}{C^2 + D^2} + \frac{BC - AD}{C^2 + D^2}i \quad (57)$$

So  $R(x + yi)$  can be expressed as:

$$R(x + yi) = \frac{A + Bi}{C + Di} = \frac{AC + BD}{C^2 + D^2} + \frac{BC - AD}{C^2 + D^2}i \quad (58)$$

Similarly,  $R(x - yi)$  can be expressed as:

$$R(x - yi) = \frac{A - Bi}{C - Di} = \frac{AC + BD}{C^2 + D^2} - \frac{BC - AD}{C^2 + D^2}i \quad (59)$$

Therefore, every transformation can be represented as a complex number.

If A, B, C, and D are real numbers and measurable physical quantities, according to de Moivre theorem:

$$\begin{aligned} & r_1 (\cos \theta_1 + i \sin \theta_1) \times r_2 (\cos \theta_2 + i \sin \theta_2) \times \cdots \times r_n (\cos \theta_n + i \sin \theta_n) \\ & = r_1 r_2 \cdots r_n \{ \cos(\theta_1 + \theta_2 + \cdots + \theta_n) + i \sin(\theta_1 + \theta_2 + \cdots + \theta_n) \} \end{aligned} \quad (60)$$

where  $r_1 = r_2 = \cdots = r_n = 1$ ,  $\theta_1 = \theta_2 = \cdots = \theta_n = \theta$ , obtain

$$(\cos \theta + i \sin \theta)^n = \cos n\theta + i \sin n\theta \quad (61)$$

where  $n$  is any positive integer, if  $z = r(\cos \theta + i \sin \theta)$ , then  $1/z = (\cos \theta - i \sin \theta)/r$ .

Another one

$$\begin{aligned} (\cos \theta + i \sin \theta)^{-n} &= (\cos \theta - i \sin \theta)^n \\ &= \{ \cos(-\theta) + i \sin(-\theta) \}^n \\ &= \cos(-n\theta) + i \sin(-n\theta) \end{aligned} \quad (62)$$

So, the de Moivre theorem holds for all positive or negative integer values of  $n$ .

Now let ABCD be the measurable value of energy, and based on the wave function  $e^{i\theta} = \cos \theta + i \sin \theta$ , we can directly convert the energy value into the form of a wave function:

$$r(\cos \theta + i \sin \theta) = \begin{cases} \frac{A + Bi}{C + Di} = \frac{AC + BD}{C^2 + D^2} + \frac{BC - AD}{C^2 + D^2} i & (B > D) \\ \frac{A - Bi}{C - Di} = \frac{AC + BD}{C^2 + D^2} - \frac{BC - AD}{C^2 + D^2} i & (D > B) \end{cases}$$

$$r(\cos \theta - i \sin \theta) = \begin{cases} \frac{A + Bi}{C + Di} = \frac{AC + BD}{C^2 + D^2} + \frac{BC - AD}{C^2 + D^2} i & (D > B) \\ \frac{A - Bi}{C - Di} = \frac{AC + BD}{C^2 + D^2} - \frac{BC - AD}{C^2 + D^2} i & (B > D) \end{cases} \quad (63)$$

Multiplying infinite amounts of energy (phase angle) into waveform for the same amount of energy

$$\begin{aligned} & \left( \frac{A + Bi}{C + Di} \right) \times \left( \frac{A + Bi}{C + Di} \right) \times \dots \times \left( \frac{A + Bi}{C + Di} \right) \\ &= \left( \frac{AC + BD}{C^2 + D^2} + \frac{BC - AD}{C^2 + D^2} i \right)^n \\ &= r^n (\cos \theta + i \sin \theta)^n \\ &= r^n (\cos n\theta + i \sin n\theta) \\ &= r^n e^{in\theta} \end{aligned} \quad (64)$$

For different energies

$$\begin{aligned} & \left( \frac{A_1 + B_1 i}{C_1 + D_1 i} \right) \times \left( \frac{A_2 + B_2 i}{C_2 + D_2 i} \right) \times \dots \times \left( \frac{A_k + B_k i}{C_k + D_k i} \right) \\ &= \left( \frac{A_1 C_1 + B_1 D_1}{C_1^2 + D_1^2} + \frac{B_1 C_1 - A_1 D_1}{C_1^2 + D_1^2} i \right) \times \dots \times \left( \frac{A_k C_k + B_k D_k}{C_k^2 + D_k^2} + \frac{B_k C_k - A_k D_k}{C_k^2 + D_k^2} i \right) \\ &= r_1 (\cos \theta_1 + i \sin \theta_1) \times r_2 (\cos \theta_2 + i \sin \theta_2) \times \dots \times r_k (\cos \theta_k + i \sin \theta_k) \\ &= r_1 r_2 \dots r_k \{ \cos (\theta_1 + \theta_2 + \dots + \theta_k) + i \sin (\theta_1 + \theta_2 + \dots + \theta_k) \} \end{aligned} \quad (65)$$

Let ABCD be the measurable value of energy, based on the energy values calculated in **Table 3**, that is  $B = \delta V_{bc}^{Antibonding}(\vec{r}_i)$ ,  $D = \delta V_{bc}^{Antibonding}(\vec{r}_j)$ ,

$A = C = \delta V_{bc}^{bonding}(\vec{r}_{ij})$ , for example, in the heterojunction MoS<sub>2</sub>/WSe<sub>2</sub>,  $B = 0.1626$ ,

$D = 1.7120$ ,  $A = C = -0.5590$  be substituted into **Eq. 63** :

$$\frac{A + Bi}{C + Di} = \frac{AC + BD}{C^2 + D^2} + \frac{BC - AD}{C^2 + D^2}i = 0.1822 + 0.2670i$$

Therefore, the measurable value of energy is represented as a complex number. Now, convert the energy value directly into the form of a wave function  $r(\cos \theta + i \sin \theta) = re^{i\theta}$ . The modulus  $r$  and radiation angle  $\theta$  are calculated using the following formula:

$$r = \sqrt{x^2 + y^2}$$

$$\theta \begin{cases} x > 0, \arctan(y/x) \\ x = 0, y > 0; \\ x = 0, y < 0; \\ x < 0, \arctan(y/x) + \pi \end{cases}$$

(66)

that is

$$0.1822 + 0.2670i = 0.3233(\cos 0.97 + i \sin 0.97)$$

Substitute into **Eq. 64**, the wave function  $r^n e^{in\theta} = 0.3233^n (\cos 0.97n + i \sin 0.97n)$  can be obtained.

Now, substitute the energy values of six different substances, MoS<sub>2</sub>/MoSe<sub>2</sub>, MoS<sub>2</sub>/MoTe<sub>2</sub>, WSe<sub>2</sub>/MoTe<sub>2</sub>, WS<sub>2</sub>, WSe<sub>2</sub>, and WTe<sub>2</sub>, into **Eq. 63** obtained:

$$\begin{cases} 0.1822 + 0.2670i = 0.3233(\cos 0.97 + i \sin 0.97) \\ 0.1143 + 0.2268i = 0.2540(\cos 1.10 + i \sin 1.10) \\ 0.5490 + 0.2953i = 0.6233(\cos 0.49 + i \sin 0.49) \\ 0.3792 + 0.3140i = 0.4924(\cos 0.69 + i \sin 0.69) \\ 0.5375 + 0.2982i = 0.6147(\cos 0.51 + i \sin 0.51) \\ 0.7418 + 0.2111i = 0.7713(\cos 0.28 + i \sin 0.28) \end{cases}$$

as shown in **Table 5**.

**Table 5** The conformal transformation of energy obtains the argument  $\theta_k$  and amplitude  $r_k$  of the wave function

	B	D	A=C	$\frac{AC + BD}{C^2 + D^2} + \frac{BC - AD}{C^2 + D^2}i$	$\theta$ (rad )	r
MoS <sub>2</sub> /WSe <sub>2</sub>	0.1626	1.7120	-0.5590	$0.1822 + 0.2670i$	0.97	0.3233
MoS <sub>2</sub> /MoTe <sub>2</sub>	0.1374	2.4440	-0.6258	$0.1143 + 0.2268i$	1.10	0.2540
WSe <sub>2</sub> /MoTe <sub>2</sub>	0.1928	0.5421	-0.3549	$0.5490 + 0.2953i$	0.49	0.6233

WS <sub>2</sub>	0.1653	0.7502	-0.3795	0.3792 + 0.3140i	0.69	0.4924
WSe <sub>2</sub>	0.1768	0.5122	-0.3303	0.5375 + 0.2982i	0.51	0.6147
WTe <sub>2</sub>	0.1644	0.2888	-0.2361	0.7418 + 0.2111i	0.28	0.7713

### 3.5 Fluctuation of electron mass and reduced mass

#### 3.5.1 Fluctuation of electron mass

From the Eq. 28 and Eq. 35 summary:

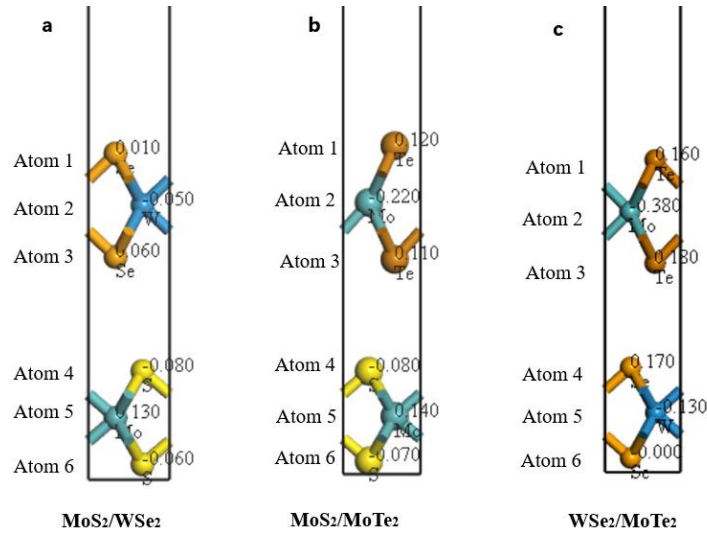
$$e_R^2 = e^2 \frac{1}{1 + \left[ \frac{e^2}{12\pi^2} \right] \ln \left( \frac{M^2}{m^2} \right)} \approx e^2 \left( 1 - \frac{e^2}{12\pi^2} \ln \frac{M^2}{m^2} \right)$$

While  $M^2$  representing the parameter of the ignorance bound, which confirms that the magnitude of the fluctuation mass of the charge is related to the imaginary mass  $M$ .

$$\Delta e^2 = \frac{e^2}{12\pi^2} \ln \frac{M^2}{m^2}$$

Among them, electronic quality  $m = 9.10956 \times 10^{-31} \text{kg}$

**Fig. 13** shows the atomic positions, types, and corresponding charges of six two-dimensional bilayer structures



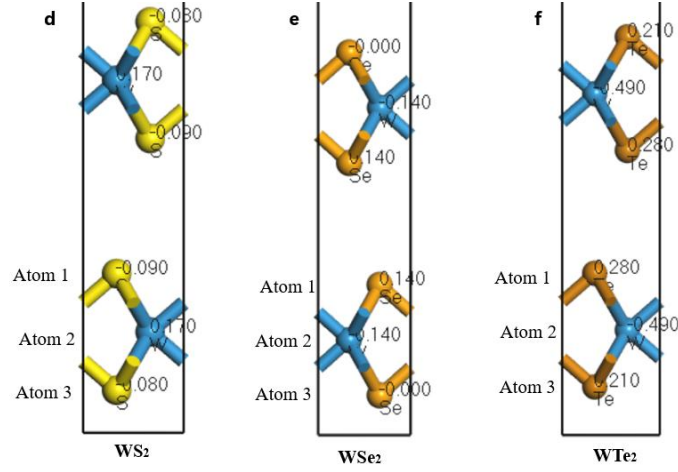


**Fig. 13** Charge transfer of MoS<sub>2</sub>/WSe<sub>2</sub>, MoS<sub>2</sub>/MoTe<sub>2</sub>, WSe<sub>2</sub>/MoTe<sub>2</sub>, WS<sub>2</sub>, WSe<sub>2</sub> and WTe<sub>2</sub>

Based on **Fig. 13**, substitute the charges of each atom into **Eq. 37** to obtain the mass fluctuations of each atom, as shown in **Table 6**

**Table 6** Fluctuation of electron mass  $M$  and charge transfer  $\Delta e$

Structure	element	$\Delta e$	$M$	
MoS <sub>2</sub> /WSe <sub>2</sub>	Atom1	Se	0.010	9.16E-31
	Atom2	W	-0.050	1.06E-30
	Atom3	Se	0.060	1.13E-30
	Atom4	S	-0.080	1.33E-30
	Atom5	Mo	0.130	2.48E-30
	Atom6	S	-0.060	1.13E-30
MoS <sub>2</sub> /MoTe <sub>2</sub>	Atom1	Te	0.120	2.14E-30
	Atom2	Mo	-0.220	1.60E-29
	Atom3	Te	0.110	1.86E-30
	Atom4	S	-0.080	1.33E-30
	Atom5	Mo	0.140	2.90E-30
	Atom6	S	-0.070	1.22E-30
WSe <sub>2</sub> /MoTe <sub>2</sub>	Atom1	Te	0.160	4.14E-30
	Atom2	Mo	-0.380	4.67E-27
	Atom3	Te	0.180	6.19E-30
	Atom4	Se	0.170	5.03E-30
	Atom5	W	-0.130	2.48E-30

	Atom6	Se	0	9.11E-31
	Atom1	S	-0.090	1.47E-30
WS <sub>2</sub>	Atom2	W	0.170	5.03E-30
	Atom3	S	-0.80	2.53E-14
	Atom1	Se	0.140	2.90E-30
WSe <sub>2</sub>	Atom2	W	-0.140	2.90E-30
	Atom3	Se	0	9.11E-31
	Atom1	Te	0.280	9.41E-29
WTe <sub>2</sub>	Atom2	W	-0.490	1.34E-24
	Atom3	Te	0.210	1.24E-29

### 3.5.2 Reduced mass of tropical geometry calculation

By combining tropical geometry with the reduced mass equation in Schrödinger's equation, we propose a way to re-characterize the reduced mass using tropical operations. Expressing the reduced mass  $-\hbar^2\bar{M}$  and potential energy terms  $E_k$  as tropical polynomials:

$$f(x, y) = \hat{E}_k x^2 + \hat{E}_k y^2 \quad (67)$$

considering that the eigenvalues  $E_k$  of the corresponding tropical geometric matrix

$$A = \begin{bmatrix} E_k & 0 \\ 0 & E_k \end{bmatrix} \text{ correspond to chemical bonds } \delta V_{bc}^{bonding}(\vec{r}_{ij}), \text{ we have:}$$

$$E_k = \delta V_{bc}^{bonding}(\vec{r}_{ij})$$

Thus, the chemical bond Mo-S correspondence matrix in the heterojunction MoS<sub>2</sub>/WSe<sub>2</sub> is:

$$A = \begin{bmatrix} -0.5590 & 0 \\ 0 & -0.5590 \end{bmatrix}$$

The tropical geometric quadratic polynomial corresponding to this  $(2 \times 2)$  matrix is:

$$f(x, y) = -0.5590x^2 - 0.5590y^2 = \hbar^2\bar{M}$$

Similarly to MoS<sub>2</sub>/MoTe<sub>2</sub>, WSe<sub>2</sub>/MoTe<sub>2</sub>, WS<sub>2</sub>, WSe<sub>2</sub> and WTe<sub>2</sub>, a tropical gradient map can be further constructed to display the gradient relationship between



reduced mass  $-\hbar^2\bar{M}$ , potential energy  $E_k$ , and their corresponding tropical matrices  $A$ , as shown in **Fig. 14**.

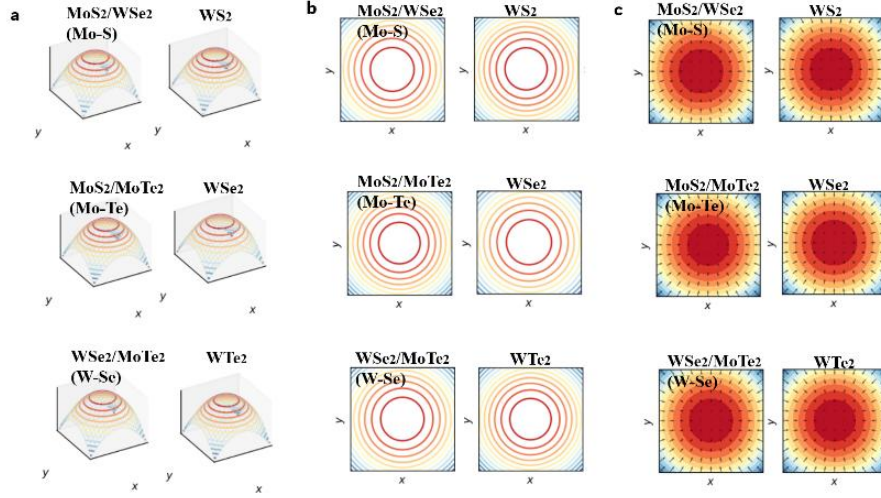


**Fig. 14** Tropical gradient map of MoS<sub>2</sub>/WSe<sub>2</sub>, MoS<sub>2</sub>/MoTe<sub>2</sub>, WSe<sub>2</sub>/MoTe<sub>2</sub>, WS<sub>2</sub>, WSe<sub>2</sub> and WTe<sub>2</sub>

The 3D surface maps of the quadratic polynomials of six heterojunctions, illustrated in **Fig. 14 a**, are as follows:  $f(x, y) = -0.5590x^2 - 0.5590y^2$  of Mo-S in MoS<sub>2</sub>/WSe<sub>2</sub>,  $f(x, y) = -0.6258x^2 - 0.6258y^2$  of Mo-Te in MoS<sub>2</sub>/MoTe<sub>2</sub>,  $f(x, y) = -0.3569x^2 - 0.3569y^2$  of W-Se in WSe<sub>2</sub>/MoTe<sub>2</sub>,  $f(x, y) = -0.3795x^2 - 0.3795y^2$  of WS<sub>2</sub>,  $f(x, y) = -0.3303x^2 - 0.3303y^2$  of WSe<sub>2</sub>,  $f(x, y) = -0.2361x^2 - 0.2361y^2$  of WTe<sub>2</sub>. The 2D contour plots of the function values of the quadratic polynomial, which are reduced mass  $-\hbar^2\bar{M}$  of the six heterojunctions, are shown in **Fig. 14 b**. **Fig. 14 c** depicts the vector of the gradient field based on the 2D contour map converted to reduced mass  $-\hbar^2\bar{M}$ .

#### 4. Conclusions

This study systematically investigates the electronic structure and chemical bonding properties of two-dimensional bilayer transition metal dichalcogenides (MX<sub>2</sub>, M = Mo, W; X = S, Se, Te). Using DFT in conjunction with the BBC model, we analyze the effects of atomic bonding and electronic states, focusing on the band gaps, deformation binding energies, and non-Hermitian bonding characteristics of different MX<sub>2</sub> compounds. The results show that charge transfer plays a significant role in reduced mass fluctuations, and tropical geometry analysis further contributes to the reduced mass. The heterostructures formed by different atomic layers can effectively

modulate the band gap of the two-dimensional bilayer transition metal dichalcogenides. All compounds exhibit semiconductor properties, with band gaps varying within a certain range. The electronic band structure and DOS reflect the orbital characteristics and interactions of the electrons. The *d* orbitals of M and *p*-orbitals of X primarily contribute to the electronic states near the Fermi level, with orbital hybridization playing a crucial role in bond formation. This study provides a theoretical foundation for further exploration of these materials, especially in electronic devices and optoelectronic applications. Future research may focus on optimizing heterostructures and exploring the properties of other transition metal dichalcogenide systems.

### References:

- [1] Y. Li, F. Wu, J. Qian, M. Zhang, Y. Yuan, Y. Bai, C. Wu, Metal chalcogenides with heterostructures for high - performance rechargeable batteries, *Small Science* 1 (2021) 2100012.
- [2] X. Liu, F. Xu, Z. Li, Z. Liu, W. Yang, Y. Zhang, H. Fan, H.Y. Yang, Design strategy for MXene and metal chalcogenides/oxides hybrids for supercapacitors, secondary batteries and electro/photocatalysis, *Coordination Chemistry Reviews* 464 (2022) 214544.
- [3] O. Samy, S. Zeng, M.D. Birowosuto, A. El Moutaouakil, A review on MoS<sub>2</sub> properties, synthesis, sensing applications and challenges, *Crystals* 11 (2021) 355.
- [4] Y. Tan, M. Bo, Electrostatic shielding effect and Binding energy shift of MoS<sub>2</sub>, MoSe<sub>2</sub> and MoTe<sub>2</sub> materials, arXiv preprint arXiv:2307.08035 (2023).
- [5] M. Bo, H. Li, Z. Huang, L. Li, C. Yao, Bond relaxation and electronic properties of two-dimensional Sb/MoSe<sub>2</sub> and Sb/MoTe<sub>2</sub> van der Waals heterostructures, *AIP Advances* 10 (2020).
- [6] M.U. Shahid, T. Najam, M.H. Helal, I. Hossain, S.M. El-Bahy, Z.M. El-Bahy, A. ur Rehman, S.S.A. Shah, M.A. Nazir, Transition metal chalcogenides and phosphides for photocatalytic H<sub>2</sub> generation via water splitting: a critical review, *International Journal of Hydrogen Energy* 62 (2024) 1113-1138.
- [7] D. Ge, R. Luo, X. Wang, L. Yang, W. Xiong, F. Wang, Internal and external electric field tunable electronic structures for photocatalytic water splitting: Janus transition-metal chalcogenides/C<sub>3</sub>N<sub>4</sub> van der Waals heterojunctions, *Applied Surface Science* 566 (2021) 150639.
- [8] Y. Chen, Y. Wang, Z. Wang, Y. Gu, Y. Ye, X. Chai, J. Ye, Y. Chen, R. Xie, Y. Zhou, Unipolar barrier photodetectors based on van der Waals heterostructures, *Nature Electronics* 4 (2021) 357-363.
- [9] H. Yang, A short review on heterojunction photocatalysts: Carrier transfer behavior and photocatalytic mechanisms, *Materials Research Bulletin* 142 (2021) 111406.
- [10] F. Li, G. Zhu, J. Jiang, L. Yang, F. Deng, X. Li, A review of updated S-scheme heterojunction photocatalysts, *Journal of Materials Science & Technology* 177 (2024) 142-180.
- [11] Q. Xu, S. Wageh, A.A. Al-Ghamdi, X. Li, Design principle of S-scheme heterojunction photocatalyst, *Journal of Materials Science & Technology* 124 (2022) 171-173.
- [12] S. Wang, S. Zhao, X. Guo, G. Wang, 2D material - based heterostructures for rechargeable batteries, *Advanced Energy Materials* 12 (2022) 2100864.
- [13] D.M. Kennes, M. Claassen, L. Xian, A. Georges, A.J. Millis, J. Hone, C.R. Dean, D. Basov, A.N. Pasupathy, A. Rubio, Moiré heterostructures as a condensed-matter quantum simulator, *Nature Physics* 17 (2021) 155-163.
- [14] B. Huang, M.A. McGuire, A.F. May, D. Xiao, P. Jarillo-Herrero, X. Xu, Emergent phenomena and proximity effects in two-dimensional magnets and heterostructures, *Nature Materials* 19 (2020) 1276-1289.
- [15] H. Chen, S. Teale, B. Chen, Y. Hou, L. Grater, T. Zhu, K. Bertens, S.M. Park, H.R. Atapattu, Y. Gao, Quantum-size-tuned heterostructures enable efficient and stable inverted perovskite solar cells, *Nature Photonics* 16 (2022) 352-358.
- [16] L. Ge, M. Bo, Atomic bonding states of metal and semiconductor elements, *Physica Scripta*

98 (2023) 105908.

[17] J.E. Zimmermann, M. Axt, F. Mooshammer, P. Nagler, C. Schüller, T. Korn, U. Höfer, G. Mette, Ultrafast charge-transfer dynamics in twisted MoS<sub>2</sub>/WSe<sub>2</sub> heterostructures, *ACS nano* 15 (2021) 14725-14731.

[18] Y. Balaji, Q. Smets, Á. Szabo, M. Mascaro, D. Lin, I. Asselberghs, I. Radu, M. Luisier, G. Groeseneken, MoS<sub>2</sub>/MoTe<sub>2</sub> heterostructure tunnel FETs using gated Schottky contacts, *Advanced Functional Materials* 30 (2020) 1905970.

[19] S. Hussain, S.A. Patil, D. Vikraman, I. Rabani, A.A. Arbab, S.H. Jeong, H.-S. Kim, H. Choi, J. Jung, Enhanced electrocatalytic properties in MoS<sub>2</sub>/MoTe<sub>2</sub> hybrid heterostructures for dye-sensitized solar cells, *Applied Surface Science* 504 (2020) 144401.

[20] J.F. Sierra, J. Fabian, R.K. Kawakami, S. Roche, S.O. Valenzuela, Van der Waals heterostructures for spintronics and opto-spintronics, *Nature Nanotechnology* 16 (2021) 856-868.

[21] Y. Li, J. Zhang, Q. Chen, X. Xia, M. Chen, Emerging of heterostructure materials in energy storage: a review, *Advanced Materials* 33 (2021) 2100855.

[22] P.V. Pham, S.C. Bodepudi, K. Shehzad, Y. Liu, Y. Xu, B. Yu, X. Duan, 2D heterostructures for ubiquitous electronics and optoelectronics: principles, opportunities, and challenges, *Chemical reviews* 122 (2022) 6514-6613.

[23] L. Pi, P. Wang, S.-J. Liang, P. Luo, H. Wang, D. Li, Z. Li, P. Chen, X. Zhou, F. Miao, Broadband convolutional processing using band-alignment-tunable heterostructures, *Nature Electronics* 5 (2022) 248-254.

[24] J. Heyd, G.E. Scuseria, M. Ernzerhof, Hybrid functionals based on a screened Coulomb potential, *The Journal of chemical physics* 118 (2003) 8207-8215.

[25] E.M. Stein, R. Shakarchi, *Complex analysis*, Princeton University Press 2010.

[26] R. Penrose, W. Rindler, *Spinors and space-time*, Cambridge university press 1984.

[27] T. Needham, *Visual complex analysis*, Oxford University Press 2023.

[28] A. Zee, *Quantum field theory in a nutshell*, Princeton university press 2010.

[29] D. Maclagan, B. Sturmfels, *Introduction to tropical geometry*, American Mathematical Society 2021.

[30] C. Kittel, P. McEuen, *Introduction to solid state physics*, John Wiley & Sons 2018.

[31] Y. Tan, M. Bo, Non - Hermitian Bonding and Electronic Reconfiguration of Ba<sub>2</sub>ScNbO<sub>6</sub> and Ba<sub>2</sub>LuNbO<sub>6</sub>, *Annalen der Physik* (2024) 2400040.

# Supplemental Material

## Electronic Structure, mass fluctuation and Localized Bond Properties of two-dimensional double-layer transition metal chalcogenide $\text{MX}_2$ (M = Mo, W; X = S, Se, Te) Calculated Based on Density Functional Theory and BBC model

Yaorui Tan and Maolin Bo\*

Key Laboratory of Extraordinary Bond Engineering and Advanced Materials

Technology (EBEAM) of Chongqing, Yangtze Normal University, Chongqing 408100, China

Corresponding Author: \*E-mail: bmlwd@yznu.edu.cn (Maolin Bo)

### Structural stability

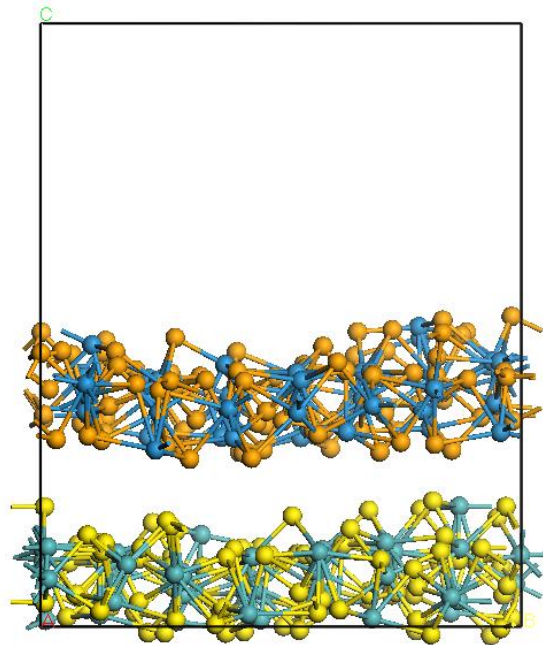
We used molecular dynamics (MD) to simulate the structural stability of two-dimensional double-layer transition metal chalcogenide  $\text{MX}_2$  (M = Mo, W; X = S, Se, Te). The  $\text{MX}_2$  structure were obtained by performing NVE ensemble with time increments at 1 fs for 100 ps (the total iteration steps are 100,000) until the potential energy accomplished a stable value. The box size and volume of two-dimensional double-layer transition metal chalcogenide  $\text{MX}_2$  (M = Mo, W; X = S, Se, Te) structure, as is shown in the Table S1. The molecular dynamics simulation results show that the structures of two-dimensional double-layer transition metal chalcogenide  $\text{MX}_2$  (M = Mo, W; X = S, Se, Te) are stable. The XRD diffraction patterns of two-dimensional double-layer transition metal chalcogenide  $\text{MX}_2$  (M = Mo, W; X = S, Se, Te)  $\text{MX}_2$  consistent with those in the database, so the crystal structure we constructed is reasonable.

**Table S1** Box size and volume two-dimensional double-layer transition metal chalcogenide  $\text{MX}_2$  (M = Mo, W; X = S, Se, Te)

Structure	Volume	Box size			Angle		
		a(Å)	b(Å)	c(Å)	$\alpha(^{\circ})$	$\beta(^{\circ})$	$\gamma(^{\circ})$
MoS <sub>2</sub> /WSe <sub>2</sub>	10172.368 Å <sup>3</sup>	22.1228	22.1228	24.000	90.000	90.000	120.000
MoS <sub>2</sub> /MoTe <sub>2</sub>	10172.368 Å <sup>3</sup>	22.1228	22.1228	24.000	90.000	90.000	60.000
WSe <sub>2</sub> /MoTe <sub>2</sub>	10970.214 Å <sup>3</sup>	22.974	22.974	24.000	90.000	90.000	60.000
WS <sub>2</sub>	10126.071 Å <sup>3</sup>	22.0724	22.0724	24.000	90.000	90.000	120.000
WSe <sub>2</sub>	10970.214 Å <sup>3</sup>	22.974	22.974	24.000	90.000	90.000	120.000
WTe <sub>2</sub>	13199.058 Å <sup>3</sup>	25.200	25.200	24.000	90.000	90.000	120.000

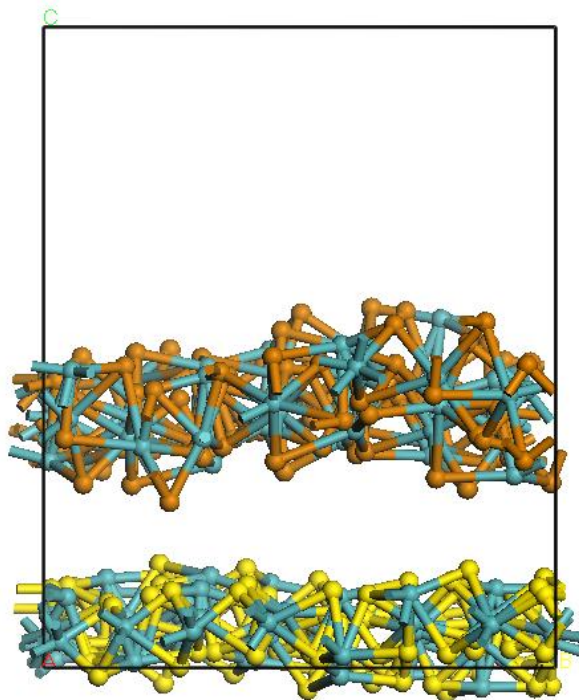
1. **Molecular dynamics (MD) to simulate the structural stability of two-dimensional double-layer transition metal chalcogenide  $\text{MX}_2$  ( $\text{M} = \text{Mo}, \text{W}$ ;  $\text{X} = \text{S}, \text{Se}, \text{Te}$ ).**

**(1) Structural stability of  $\text{MoS}_2/\text{WSe}_2$**



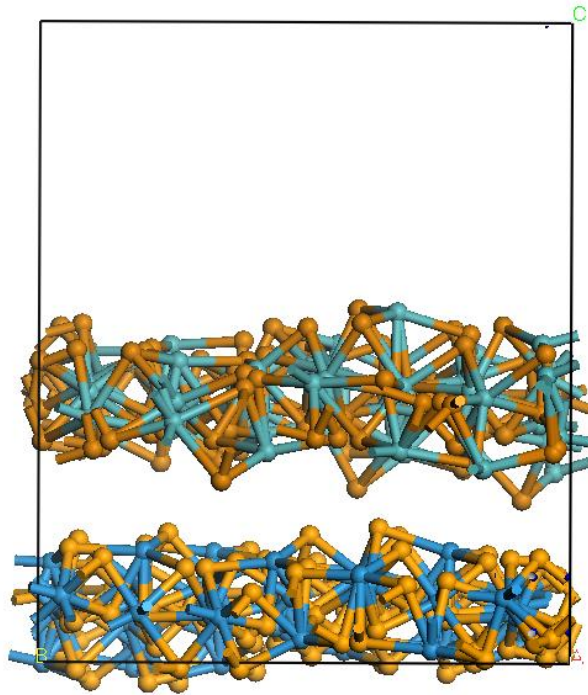
298K

**(2) Structural stability of  $\text{MoS}_2/\text{MoTe}_2$**



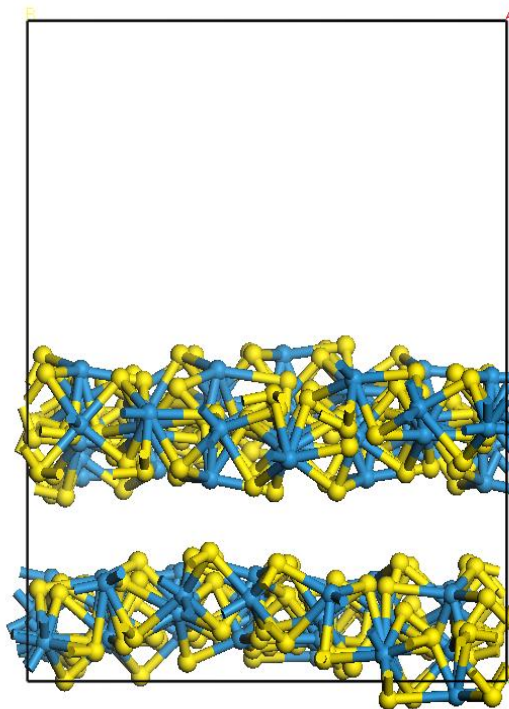
298K

(3) Structural stability of WSe<sub>2</sub>/MoTe<sub>2</sub>



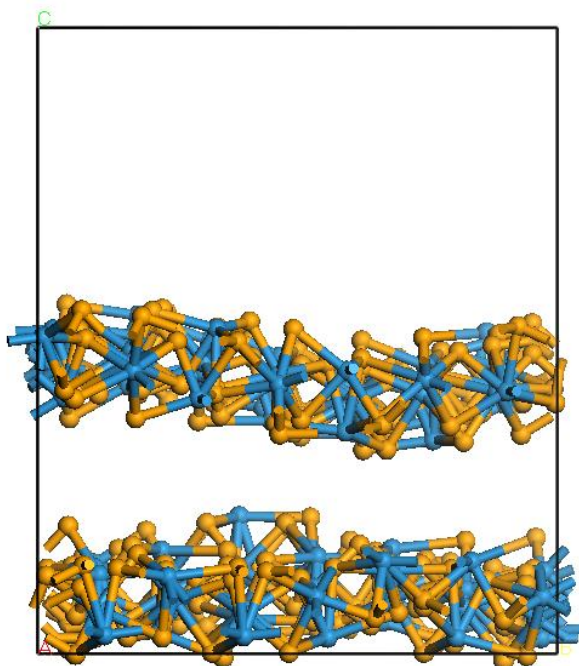
298K

(4) Structural stability of WS<sub>2</sub>



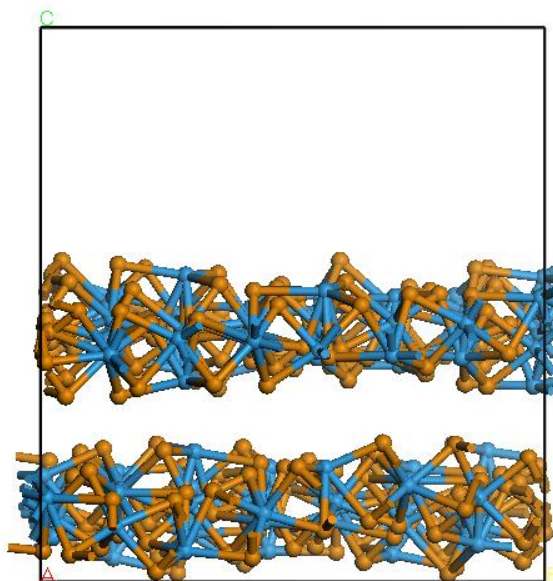
298K

(5) Structural stability of WSe<sub>2</sub>



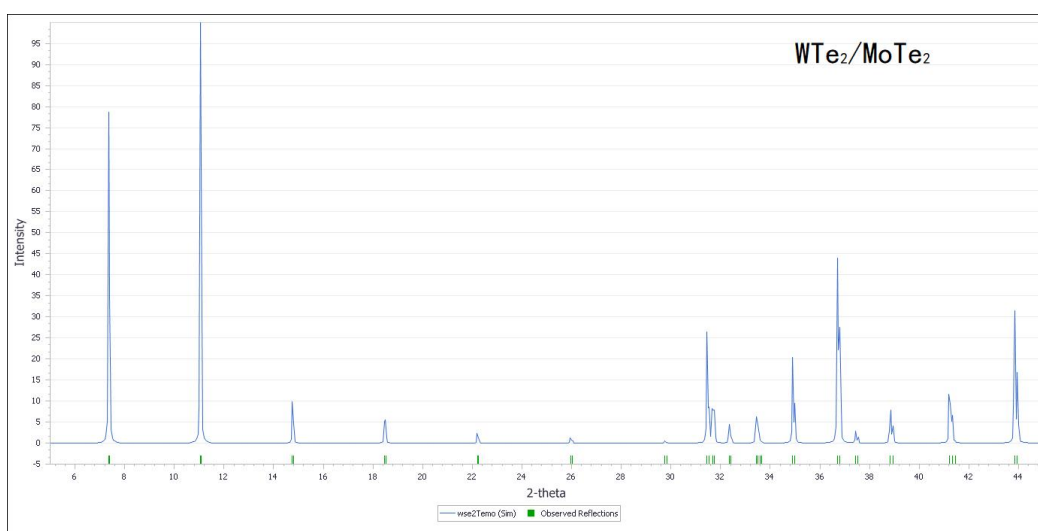
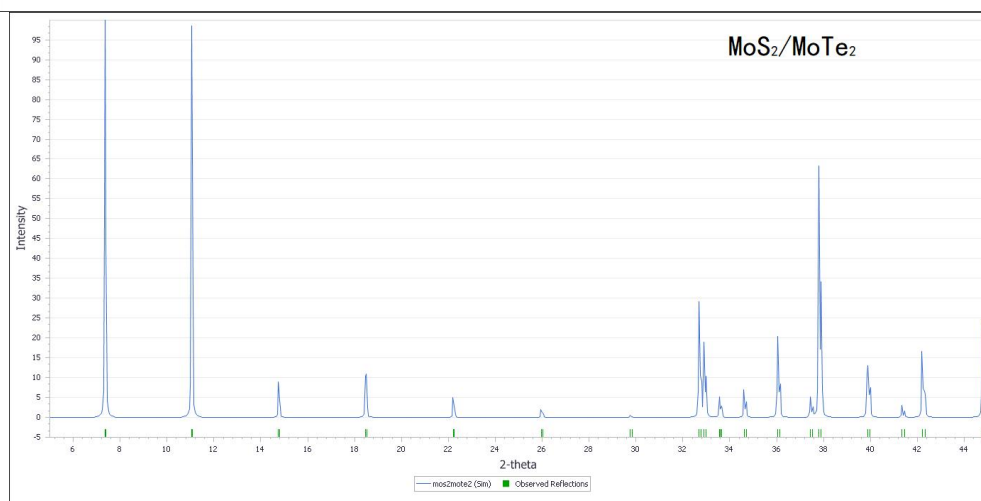
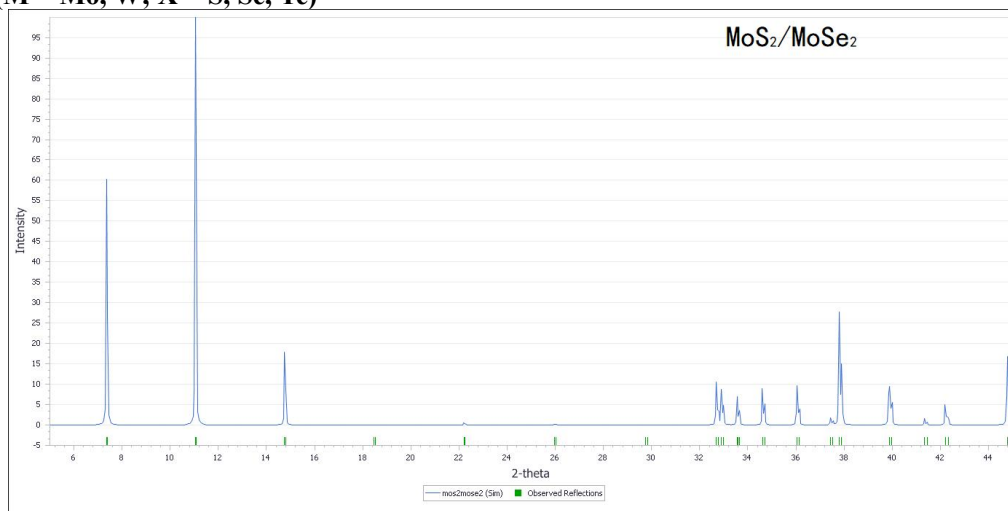
298K

(6) Structural stability of WTe<sub>2</sub>

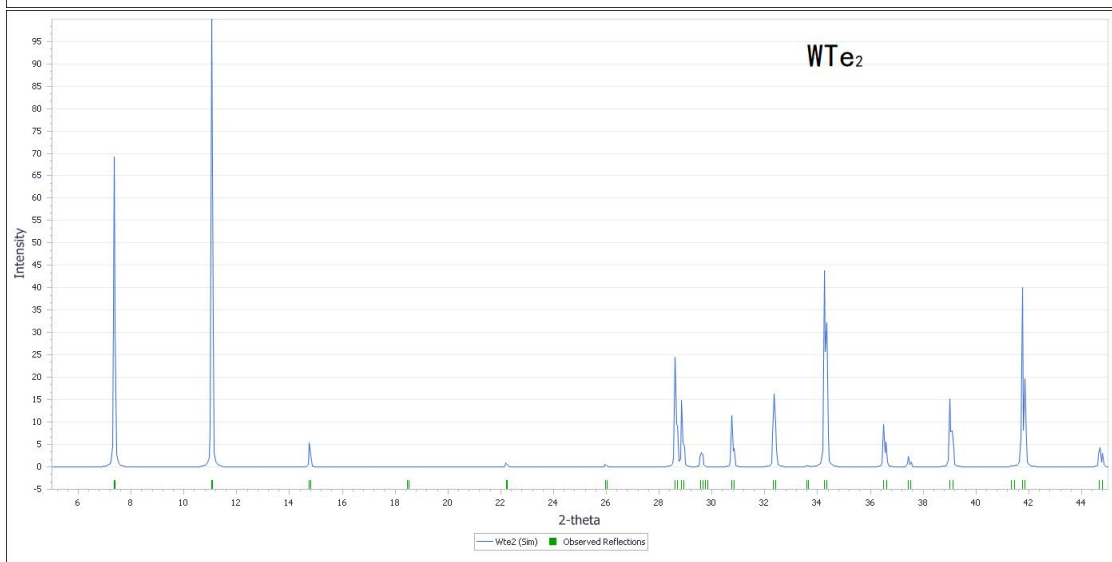
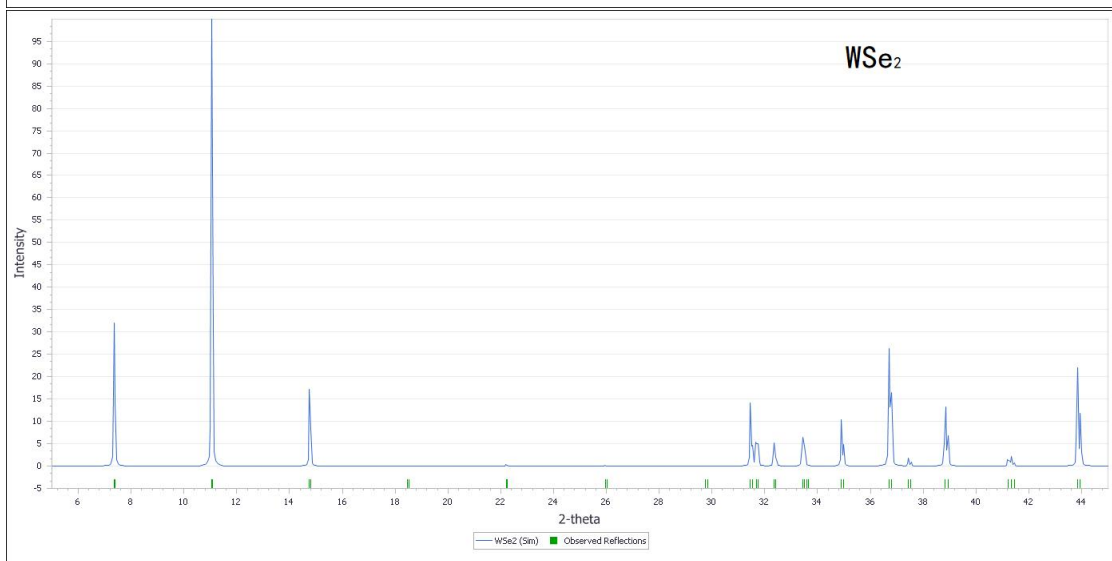
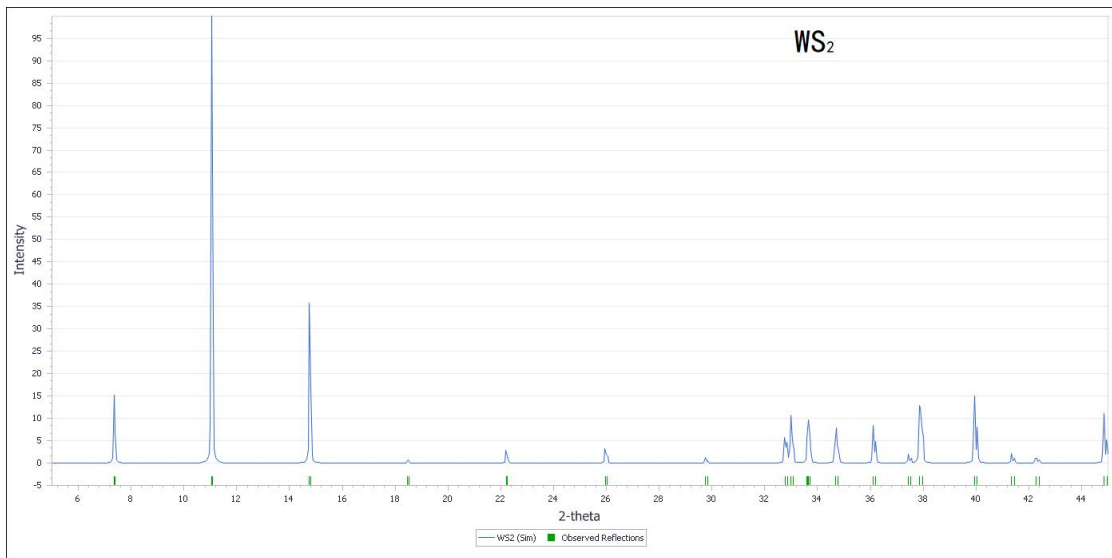


298K

## 2.XRD diffraction patterns of two-dimensional double-layer transition metal chalcogenide MX<sub>2</sub> (M = Mo, W; X = S, Se, Te)







### 3.Lorentz transformation

According to special relativity, the laws of physics hold as well in a reference frame moving at a constant velocity as they do in a stationary frame. One embarrassing result is that it is impossible to distinguish which system (if any) is stationary, so it is impossible to know the "exact" speed of any other system.

According to the theory of special relativity, the laws of physics are equally valid in all inertial frames. An inertial frame is a system that follows Newton's first law of inertia: an object maintains a constant velocity in a straight line unless a force acts on it. It is easy to see that any two inertial frames must move at a constant speed relative to each other, and any frame that moves at a constant speed relative to an inertial frame is also an inertial system.

Assuming we have two inertial frames  $S$  and  $S'$  moving relative to  $S$  at a constant velocity  $V$  (magnitude  $V$ ) ( $S$  therefore moves relative to  $S'$  at a velocity  $-V$ ). We can also take the coordinates  $x/x'$  so that the motion follows the usual axis (see Figure 1), and place the clocks of each inertial frame at the origin, so that both clocks read zero when the two frames coincide (i.e.  $x = x' = 0$ , at that time  $t = t' = 0$ ). Assuming that an event  $(x, y, z)$  occurs at time  $t$  in the  $S$  system.

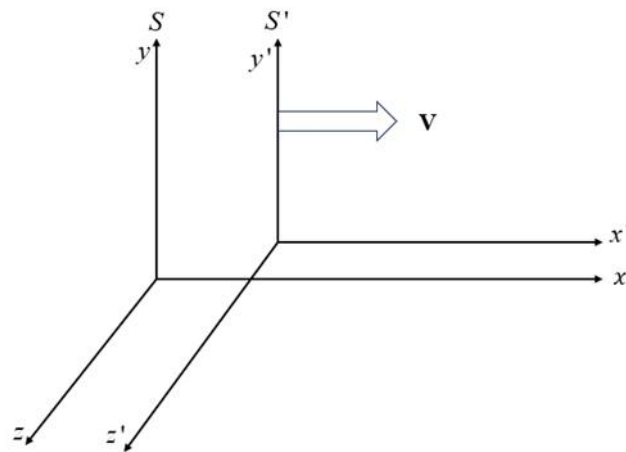


Figure 1

Question: What are the spatiotemporal coordinates  $t'$  and  $(x', y', z')$  of the same event in the  $S'$  system? The answer is provided by the Lorentz transformation:

$$x' = \gamma(x - vt)$$

$$y' = y$$

$$z' = z$$

$$t' = \gamma\left(t - \frac{v}{c^2}x\right)$$

among

$$\gamma \equiv \frac{1}{\sqrt{1 - \frac{v^2}{c^2}}}$$

The inverse exchange from  $S'$  to  $S$  can be easily changed. The symbol obtained is:

$$\begin{aligned}
x &= \gamma(x' - vt') \\
y &= y' \\
z &= z' \\
t &= \gamma\left(t' - \frac{v}{c^2}x'\right)
\end{aligned}$$

#### 4. Four vectors

We define the position time four vectors  $x^\mu$ ,  $\mu = 0, 1, 2, 3$  as follows:

$$x^0 = ct, x^1 = x, x^2 = y, x^3 = z$$

The Lorentz transformation can be written in a more symmetrical form:

$$\begin{aligned}
x^{0'} &= \gamma(x^0 - \beta x^1) \\
x^{1'} &= \gamma(x^1 - \beta x^0) \\
x^{2'} &= x^2 \\
x^{3'} &= x^3
\end{aligned}$$

among

$$\beta \equiv \frac{v}{c}$$

Tighter and more compact

$$x^{\mu'} = \sum_{\nu=0}^3 \Lambda_{\nu}^{\mu} x^{\nu}, (\mu = 0, 1, 2, 3)$$

The coefficient  $\Lambda_{\nu}^{\mu}$  can be seen as a matrix element of a matrix  $\Lambda$ :

$$\Lambda = \begin{pmatrix} \gamma & -\gamma\beta & 0 & 0 \\ -\gamma\beta & \gamma & 0 & 0 \\ 0 & 0 & 1 & 0 \\ 0 & 0 & 0 & 1 \end{pmatrix}$$

(i.e.  $\Lambda_0^0 = \Lambda_1^1 = \gamma$ ;  $\Lambda_0^1 = \Lambda_1^0 = -\gamma\beta$ ;  $\Lambda_2^2 = \Lambda_3^3 = 1$ ; all others are 0). To avoid writing too many summation signs, we will use Einstein's "summation rule", which requires automatic summation of repeated Greek indices (one subscript, one superscript) from 0 to 3. Therefore, the equation is written as follows at the end:

$$x^{\mu'} = \Lambda_{\nu}^{\mu} x^{\nu}$$

The special advantage of this neat expression is that it has the same form for Lorentz transformations that are not along the  $x$ -direction; In fact, the coordinate axes of  $S$  and  $S'$  do not even need to be parallel to each other; The matrix  $\Lambda$  is naturally more complex, but equation still holds.

When transitioning from  $S$  to  $S'$ , although the individual coordinates of the event may change, a special combination of them remains unchanged:

$$I = (x^0)^2 - (x^1)^2 - (x^2)^2 - (x^3)^2 = (x^{0'})^2 - (x^{1'})^2 - (x^{2'})^2 - (x^{3'})^2$$

The quantity that has the same value in any inertial frame is called an invariant. Similarly, if an appropriate angle  $\theta$  is chosen as the pivot (counterclockwise pivot):

$$\begin{cases} x \rightarrow x \cos \theta + y \sin \theta \\ y \rightarrow -x \sin \theta + y \cos \theta \end{cases}$$

Represent by matrix

$$\begin{pmatrix} x \\ y \end{pmatrix} \rightarrow \begin{pmatrix} x \cos \theta + y \sin \theta \\ -x \sin \theta + y \cos \theta \end{pmatrix} = \begin{pmatrix} \cos \theta & \sin \theta \\ -\sin \theta & \cos \theta \end{pmatrix} \begin{pmatrix} x \\ y \end{pmatrix}$$

Represent by matrix components

$$x'_i = R_i^j x_j, \quad x_i = \begin{pmatrix} x \\ y \end{pmatrix}, \quad i, j = 1, 2$$

Take transpose

$$(x' \ y') = (x \ y) \begin{pmatrix} \cos \theta & -\sin \theta \\ \sin \theta & \cos \theta \end{pmatrix}$$

$$x'^i = x^j (R^T)_j^i, \quad x^j = (x \ y), \quad i, j = 1, 2, \quad R_i^j x_j = R_i^1 x_1 + R_i^2 x_2$$

therefore

$$\begin{aligned} R^T R &= \begin{pmatrix} \cos \theta & -\sin \theta \\ \sin \theta & \cos \theta \end{pmatrix} \begin{pmatrix} \cos \theta & \sin \theta \\ -\sin \theta & \cos \theta \end{pmatrix} \\ &= \begin{pmatrix} \cos^2 \theta + \sin^2 \theta & \cos \theta \sin \theta - \sin \theta \cos \theta \\ \sin \theta \cos \theta - \cos \theta \sin \theta & \cos^2 \theta + \sin^2 \theta \end{pmatrix} \\ &= \begin{pmatrix} 1 & 0 \\ 0 & 1 \end{pmatrix} = I \end{aligned}$$

So  $r^2 = x^2 + y^2 + z^2$  remains constant under rotation.

Now, I want to write this invariant in the form of summation:  $\sum_{\mu=0}^3 x^\mu x^\mu$ , but

unfortunately there are three repeated negative signs for summation. To preserve their traces, we introduce a metric  $g_{\mu\nu}$  whose components can be displayed as a matrix  $g$ :

$$g = \begin{pmatrix} 1 & 0 & 0 & 0 \\ 0 & -1 & 0 & 0 \\ 0 & 0 & -1 & 0 \\ 0 & 0 & 0 & -1 \end{pmatrix}$$

(i.e.  $g_{00} = 1; g_{11} = g_{22} = g_{33} = -1$ , all others are 0). With the help of  $g_{\mu\nu}$ , invariants  $I$  can be written in the form of double sums:

$$I = \sum_{\mu=0}^3 \sum_{\nu=0}^3 g_{\mu\nu} x^\mu x^\nu = g_{\mu\nu} x^\mu x^\nu$$

Furthermore, we define covariant four vectors  $x_\mu$  (with indicators listed below) as follows:

$$x_\mu \equiv g_{\mu\nu} x^\nu$$

(That is,  $x_0 = x^0, x_1 = -x^1, x_2 = -x^2, x_3 = -x^3$ ). To emphasize the difference, we call the "original" four vector  $x^\mu$  (with the index above) the inverted four vector. Invariants can therefore be written in the simplest form:

$$I = x^\mu x_\mu$$

(Or equivalently written  $x_\mu x^\mu$ ). Once you get used to this method, it will become very simple. (Furthermore, it effectively extends non-Cartesian coordinate systems to the curved spaces encountered in general relativity, although neither of these things are relevant to us here.)

Bit-time four vectors  $x^\mu$  are typical of all four vectors. When we change from one inertial space to another, we define four vectors  $a^\mu$  as a four component quantity to transform in the same

way as  $x^\mu$ , that is:

$$a^{\mu'} = \Lambda_{\nu}^{\mu} a^{\nu}$$

Using the same coefficient  $\Lambda_{\nu}^{\mu}$ . For each of these (inverse) four vectors, we introduce a covariant four vector  $a_{\mu}$  by changing the sign of its spatial component

$$a_{\mu} = g_{\mu\nu} a^{\nu}$$

Of course, we can also reverse from co empty to inverse by changing the symbol again:

$$a^{\mu} = g^{\mu\nu} a_{\nu}$$

Technically, this  $g^{\mu\nu}$  is the element of a matrix  $g^{-1}$  (however, since our metric is its own inverse,  $g^{\mu\nu}$  and  $g_{\mu\nu}$  are the same). Given any two four vectors,  $a^{\mu}$  and  $b^{\mu}$ :

$$a^{\mu} b_{\mu} = a_{\mu} b^{\mu} = a^0 b^0 - a^1 b^1 - a^2 b^2 - a^3 b^3$$

It is invariant (with the same value in any inertial frame). We will call it the scalar product of  $a$  and  $b$ : this is the four-dimensional analogue corresponding to the dot product of two three vectors (a four-dimensional analogue without cross product).

If you don't want to write subscripts, you can use dot product instead. Position vector dot product:

$$\vec{x} \cdot \vec{x} = x^i x_i = \delta_{ij} x^i x^j = (x \ y) \begin{pmatrix} x \\ y \end{pmatrix} = x^2 + y^2$$

Denoted  $\Lambda$  as Lorentz transformation matrix:

$$S^2 = x^{\mu} x_{\mu} = g_{\mu\nu} x^{\mu} x^{\nu} = g_{\rho\sigma} x^{\rho} x^{\sigma}$$

$$S'^2 = x'^{\mu} x'_{\mu} = g_{\mu\nu} x'^{\mu} x'^{\nu} = g_{\mu\nu} \Lambda_{\rho}^{\mu} x^{\rho} \Lambda_{\sigma}^{\nu} x^{\sigma}$$

The transformation that satisfies the following conditions is called Lorentz transformation:

$$S^2 = S'^2 \Rightarrow g_{\rho\sigma} = g_{\mu\nu} \Lambda_{\rho}^{\mu} \Lambda_{\sigma}^{\nu}$$

So, it can be written as:

$$g_{\rho\sigma} = g_{\mu\nu} \Lambda_{\rho}^{\mu} \Lambda_{\sigma}^{\nu} = (\Lambda^T)_{\rho}^{\mu} g_{\mu\nu} \Lambda_{\sigma}^{\nu}$$

It can be written in the form of a matrix:

$$\Lambda^T g \Lambda = g = \begin{pmatrix} -1 & & & \\ & -1 & & \\ & & -1 & \\ & & & -1 \end{pmatrix}$$

The transformation matrix form is as follows:

$$\begin{pmatrix} 1 & & & \\ & 1 & & \\ & \cos \theta_x & -\sin \theta_x & \\ & \sin \theta_x & \cos \theta_x & \end{pmatrix}, \begin{pmatrix} 1 & & & \\ & \cos \theta_y & \sin \theta_y & \\ & & 1 & \\ & -\sin \theta_y & \cos \theta_y & \end{pmatrix}$$

$$\begin{pmatrix} 1 & & & \\ & \cos \theta_z & -\sin \theta_z & \\ & -\sin \theta_z & \cos \theta_z & \\ & & & 1 \end{pmatrix}, \begin{pmatrix} \cosh Y_x & -\sinh Y_x & & \\ -\sinh Y_x & \cosh Y_x & & \\ & & & 1 \\ & & & & 1 \end{pmatrix}$$

$$\begin{pmatrix} \cosh Y_y & -\sinh Y_y & & \\ & 1 & & \\ -\sinh Y_y & & \cosh Y_y & \\ & & & 1 \end{pmatrix}, \begin{pmatrix} \cosh Y_z & -\sinh Y_z & & \\ & 1 & & \\ & & 1 & \\ -\sinh Y_z & & & \cosh Y_z \end{pmatrix}$$

therefore

$$\cosh Y_x = \frac{1}{\sqrt{1-v^2}}, \quad \sinh Y_x = \frac{v}{\sqrt{1-v^2}}$$

Obtain transformation:

$$x \rightarrow \Lambda^{-1}x = \frac{x+vt}{\sqrt{1-v^2}}, \quad t \rightarrow \Lambda^{-1}t = \frac{t+vx}{\sqrt{1-v^2}},$$

Equivalent to:

$$x \rightarrow x+vt, t \rightarrow t'$$

The Lorentz inverse transform satisfies the form:

$$x'^{\mu} = \Lambda_{\nu}^{\mu} x^{\nu}, \quad x^{\nu} = (\Lambda^{-1})^{\mu}_{\nu} x'^{\mu}$$

Orthogonality

$$\begin{aligned} x'^{\mu} &= \Lambda_{\nu}^{\mu} x^{\nu} = \Lambda_{\nu}^{\mu} (\Lambda^{-1})^{\rho}_{\nu} x'^{\rho} = \delta_{\nu}^{\rho} x'^{\nu}, \Lambda_{\nu}^{\mu} (\Lambda^{-1})^{\nu}_{\rho} = \delta_{\rho}^{\mu} \\ g_{\rho\sigma} (\Lambda^{-1})^{\rho}_{\tau} &= g_{\mu\nu} \Lambda_{\rho}^{\mu} \Lambda_{\sigma}^{\nu} (\Lambda^{-1})^{\rho}_{\tau} = g_{\mu\nu} \Lambda_{\sigma}^{\nu} \delta_{\tau}^{\mu} = g_{\tau\nu} \Lambda_{\sigma}^{\nu} \\ g^{\gamma\sigma} g_{\gamma\sigma} (\Lambda^{-1})^{\rho}_{\tau} &= \delta_{\rho}^{\tau} (\Lambda^{-1})^{\rho}_{\tau} = g^{\gamma\sigma} g_{\gamma\sigma} \Lambda_{\sigma}^{\nu} \Rightarrow (\Lambda^{-1})^{\gamma}_{\tau} g^{\gamma\sigma} g_{\gamma\sigma} \Lambda_{\sigma}^{\nu} \\ x'^{\mu} &= g_{\mu\nu} x'^{\nu} = g^{\mu\nu} x_{\rho} \Lambda_{\nu}^{\rho} = g^{\mu\nu} \Lambda_{\nu}^{\rho} g_{\mu\nu} x^{\sigma} = (\Lambda^{-1})^{\mu}_{\sigma} x^{\sigma}, \phi(x') \rightarrow \phi(x) \\ V^{\mu}(x) &\rightarrow \Lambda_{\nu}^{\mu} V^{\nu}(x) = \Lambda_{\nu}^{\mu} V^{\nu}(\Lambda^{-1}x) \end{aligned}$$

Classify all four vectors by symbol:

$$\Lambda^{\mu} V_{\mu} \begin{cases} > 0, \textit{timelike} \\ < 0, \textit{spacelike} \\ = 0, \textit{lightlike} \end{cases}$$

Starting from vectors, we arrive at tensors in a short step: a second-order tensor  $s^{\mu\nu}$  carrying two indicators, there are  $4^2 = 16$  components, and two transformations  $\Lambda$ :

$$s'^{\mu\nu} = \Lambda_{\kappa}^{\mu} \Lambda_{\sigma}^{\nu} s^{k\sigma}$$

A third-order tensor  $t^{\mu\nu\lambda}$  carries three indicators, there are  $4^3 = 64$  components, and is transformed using three transformations  $\Lambda$ :

$$t'^{\mu\nu\lambda} = \Lambda_{\kappa}^{\mu} \Lambda_{\sigma}^{\nu} \Lambda_{\tau}^{\lambda} t^{k\sigma\tau}$$

In these hierarchies, vectors are tensors of order 1, and scalars (invariant) are tensors of order 0. We construct covariant and "mixed" tensors by reducing the indicators (at the cost of adding a negative sign to each spatial indicator), for example

$$s_{\nu}^{\mu} = g_{\nu\lambda} s^{\mu\lambda}; s_{\mu\nu} = g_{\mu\kappa} g_{\nu\lambda} s^{k\lambda}$$

Note that the product of two tensors itself is also a tensor:  $(a^{\mu} b^{\nu})$  is a second-order tensor;  $(a^{\mu} t^{\nu\lambda\sigma})$  is a fourth-order tensor; wait. Finally, we can "shrink" any  $n+2$  order tensor into an

n-order tensor by summing a pair of upper and lower indices. Therefore,  $s_{\mu}^{\mu}$  is a scalar;  $t_{\nu}^{\mu\nu}$  is a vector;  $a_{\mu} t^{\mu\nu\lambda}$  is a second-order tensor.